Thesis for the Degree of Licentiate of Engineering

Alloy Plasmonics

Fundamentals and Application in Catalysis

Christopher Tiburski

Department of Physics
CHALMERS UNIVERSITY OF TECHNOLOGY
Gothenburg, Sweden 2020

Alloy Plasmonics - Fundamentals and Application in Catalysis
Christopher Tiburski

Department of Physics
Chalmers University of Technology
SE-412 96 Gothenburg
Sweden
Telephone + 46 (0)31-772 1000

Printed at Chalmers Reproservice Göteborg, Sweden 2020

Alloy Plasmonics - Fundamentals and Application in Catalysis

Christopher Tiburski
Department of Physics
Chalmers University of Technology

Abstract

Alloys have for a long time been important in the development of our society; from the bronze age, where man learned how to alloy copper with tin, to today, where many products are made of steel and aluminum alloys. Similarly, but maybe not as generally well known, also in heterogeneous catalysis alloys are explored to develop solutions to increase activity and selectivity of chemical processes. Furthermore, alloys have lately been proposed as a new paradigm in nanophotonics, as a means to tailor optical properties of nanomaterials that find applications within telecommunication, sensing, or biotechnology. Nanophotonics and catalysis, separately and in combination, are the focus of this thesis. Specifically, we have compiled a library of alloy complex dielectric functions for the late transition metals by utilizing time-dependent density-functional theory. The calculated dielectric functions were benchmarked by (i) nanofabricating series of alloy nanoparticle arrays with systematically varying composition, (ii) measuring their plasmonic properties, and (iii) comparing these properties with electrodynamic simulations of alloy nanoparticles, using the dielectric function library as the input. The second theme in this thesis is plasmon-enhanced catalysis. In this field there is a continuous discussion regarding the reaction enhancing mechanisms when noble metal catalyst nanoparticles are irradiated with visible light during a catalytic reaction. Here we investigated the role of photothermal enhancement of reactions by tailoring the catalytic activity of nanofabricated particles without radiation by means of alloying Pd with Au, while keeping the optical absorption cross-section constant, as confirmed by electrodynamics simulations using our dielectric function library as the input.

Keywords: nanoalloys, nanofabrication, nanoparticles, LSPR, heterogeneous catalysis, dielectric function, light, CO oxidation, palladium, gold

List of appended papers

This thesis is based on the work presented in the following papers:

Paper I

A Library of Late Transition Metal Alloy Dielectric Functions for Nanophotonic Applications.

J. M. Rahm*, C. Tiburski*, T. P. Rossi, F. A. A. Nugroho, S. Nilsson, C. Langhammer, P. Erhart.

Advanced Functional Materials **30**, 2002122 (2020).

* equal contribution

Paper II

Light-Off in Plasmon-Mediated Photocatalysis.

C. Tiburski, S, Nilsson, Z. Say, J. Fritzsche, C. Langhammer

In Manuscript

Contents

1 Introduction

Alloys have been important for the development of society for a long time. The most prominent example from history is probably the bronze age, where man started to alloy copper with tin, which provided tools with increased hardness, stiffness or ductility, depending on the composition. The situation is similar today, as the properties of metals like iron are modified by mixing it with carbon to form steel. The properties of steel can be further tailored for specific applications by, for example, mixing it with chromium to improve toughness, with manganese to increase wear resistance, or with titanium to improve corrosion resistance[1].

At the same time, the concept of alloying is also explored in younger areas of science and technology, like in the field of nanophotonics[2]. In this area, alloying has recently been proposed as a means to tailor optical properties of nanomaterials, to achieve functions and properties that are not accessible when using pure elements alone - conceptually very similar as for iron when making steel. However, the use of alloys in nanophotonic applications is still in its infancy due to a lack of understanding of the fundamental optical properties of alloys in general, and a lack of complex dielectric functions of alloys that cover a wide spectral and compositional range in particular. The latter is critical since, projected onto nanophotonics, dielectric functions are a key resource for being able to predict the response of nanostructures to light by means of modelling or electrodynamic simulations. Such predictions, in turn, are important to both rationally design and fine-tune alloy nanostructures for their intended applications, such as waveguides, gratings or plasmonic nanoantennas.

In response, in **Paper I**, we have compiled a library of complex dielectric functions for alloys of the late transition metals by utilizing time-dependent density-functional theory. We have then benchmarked the dielectric functions calculated from first

principles by nanofabricating series of alloy nanoparticles, measuring their plasmonic properties and comparing these properties with electrodynamic simulations using the derived dielectric functions as the key input. The found excellent agreement between theory and experiment corroborated the validity of our dielectric functions, which thereby finally provide the community with a consistent data set across a wide spectral range and without limitations in alloy composition.

As a second key aspect of this thesis, I want to highlight that nanomaterials and structures not only find application in nanophotonics but also in heterogeneous catalysis, where they constitute the workhorse in a quest to increase the yield and reduce the environmental impact of chemical processes. To pinpoint the importance of this quest, we remind ourselves that ca. 90% of the chemical industry uses a catalytic reaction somewhere along their value chain[3]. An interesting concept related to these efforts is to use light and its interaction with solid state nanomaterials as a means to increase catalyst activity or steer selectivity. This area of technology is commonly referred to as photocatalysis[4]. In recent years, a sub-area of photocatalysis has developed rapidly, which proposes the use of so-called localized surface plasmon resonances (LSPR) to enhance the cross section of photocatalytic reactions on metal nanoparticles. LSPR are resonant collective free electron oscillations in metal nanoparticles excited by visible light. This branch of nanoscience at the interface between nanophotonics and heterogeneous catalysis is commonly referred to as plasmon-mediated catalysis. Despite its rapid development with sometimes spectacular reports about rate and selectivity enhancements of plasmonic catalysts[5,6,7], there is a discussion about the mechanistic origin of the observed effects, and in particular the distinction between photothermal and hot-carrier mediated effects has developed into a "holy grail" of the field[8,9].

In **Paper II**, we studied such photothermal effects that arise upon noble metal catalyst nanoparticle irradiation with visible light during a catalytic reaction. Specifically, we applied the concept of alloying, by mixing palladium with gold in arrays of nanofabricated catalyst particles, to tailor the catalytic activity of our model system in the dark, while, at the same time, maintaining a constant optical cross-section upon illumination. In this way, we are able to unambiguously show that the catalytic activity is not governed by the photon flux alone but also depends strongly on the temperature of the catalyst in the dark.

2 Alloys

2.1 Phase Diagrams

Alloys are the combination of two or more components, intermixed at the atomic level, where at least one is a metal[10]. They are widely used in different technologies to alter material properties like increasing the strength and hardness[11]. They are furthermore explored in heterogeneous catalysis to optimize activity and selectivity, and predicted to find application in plasmon-mediated catalysis as a means to tailor the light harvesting capabilities of metal nanoparticles. Overall, alloys provide ample opportunity to tailor functional material properties and to achieve functions not obtainable by the constituent materials alone.

When designing alloys, the phase diagram for the constituent materials should be consulted. For a unary system the phase diagram shows the phase and phase changes of the system depending on temperature and pressure. In the case of binary alloys, the phase diagram usually shows the phase and phase changes depending on temperature and alloy composition for constant pressure (usually 1 atm). It is also worth noting that phase diagrams represent the system at equilibrium. Therefore, using high heating and cooling rates will change the phase diagram. Melting points will, for example, appear shifted, since the system may be kinetically trapped in a state different from the equilibrium one.

Focusing now on metals only, which are the systems of relevance for my work, the most common phases of an alloy are a solid solution and intermetallic phase. In a solid solution, the element B, the *solute* is dissolved in the crystal lattice of element A, the *solvent*. The phase structure of the solid solution is the same as the one of the solvent[12]. The limit of solid solubility depends on the similarity and

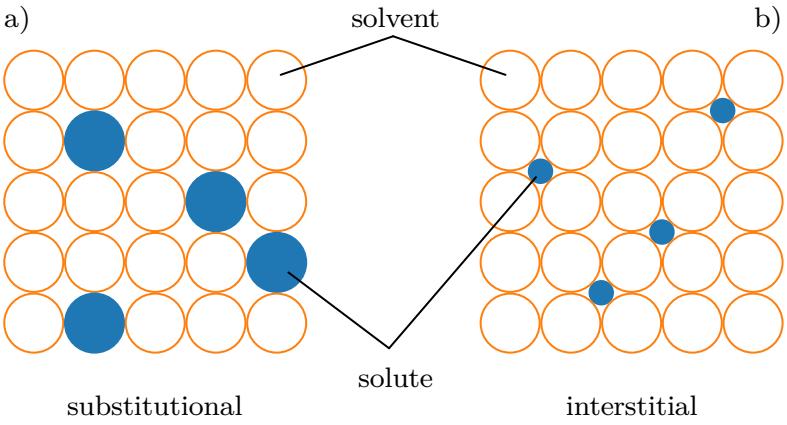

Figure 2.1: a) Schematic depiction of a substitutional alloy, where the solute substitutes a solvent atom. b) Schematic depiction of an interstitial alloy, where the solute atoms sit between the solvent atoms in interstitial lattice sites.

difference between the atoms of solute and solvent[12]. If they have a similar size and the solute atoms replace the solvent atoms, the solid solution is called substitutional (Figure 2.1a). According to the *Hume-Rothery-rules*[13], the atoms can deviate a maximum of 15% in size to form a substitutional solid solution. In addition to size requirements, the chemical affinity, relative valency and lattice type need to be taken into account. If, for example, the elements have very different electronegativities, they tend to form a compound instead of an alloy, with polar covalent bonds between its constituents. Finally, it is important to mention that these are general rules with many exceptions. However, they give a qualitative estimate if two atoms would form a substitutional solid solution. If the difference in radius of the atoms is big enough, an interstitial solid solution will form instead, where the solute atoms occupy interstitial sites of the solvent (Figure 2.1b).

In phase diagrams, solid solutions are often denoted with a lowercase Greek letter. In Figure 2.2 that depicts the binary phase diagram for silver and copper, this is denoted α and β. If it is not possible for a particular composition to form either an α or β phase, a mixture of both is formed, as also indicated in Figure 2.2. This two-phase coexistence region is denoted as $\alpha + \beta$, where both phases are saturated at equilibrium. The amount of each phase in the mixed phase can be calculated

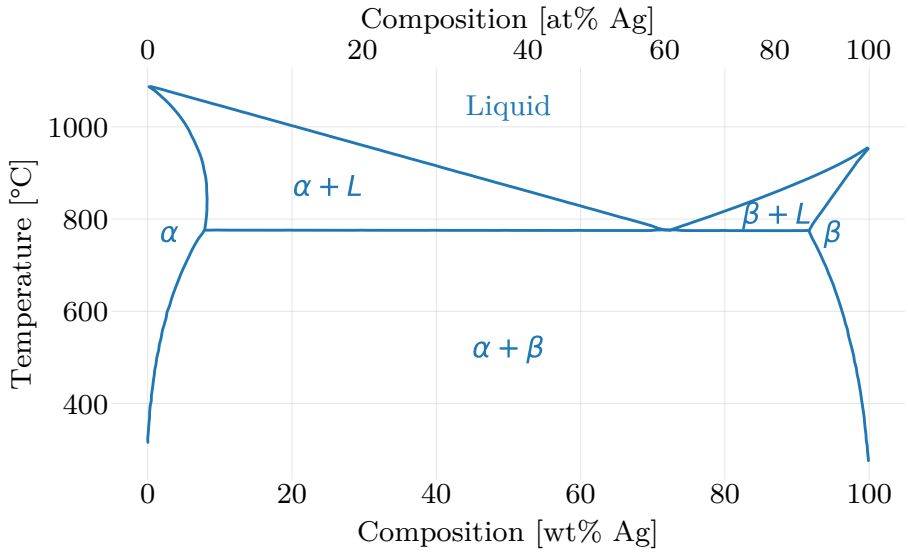

Figure 2.2: Phase diagram of silver-copper. The α and β phases are at both sides of the diagram, at high copper and silver concentrations, respectively. The largest part of the phase diagram in the center corresponds to a two-phase coexistence region, where the α and β phase are present simultaneously. L denotes the liquid phase. In the regions $\alpha + L$ and $\beta + L$ coexist the solid with the liquid phase. The data are from Kawecki et al.[14]

using the *Lever* rule[11]. Finally, a region where an alloy does not fully mix is called a miscibility gap. If the crystal structure of an alloy differs from both constituents', it is called an intermetallic compound or intermetallic phase.

An example of a very simple phase diagram is the one for silver-gold (Figure 2.3). This system forms a random alloy throughout the whole composition range and has a small area between the liquidus and solidus lines, where liquid and solid phases coexist.

There are several ways to fabricate bulk alloys from their constituents. One way is to mix the elements in liquid form, which works well for metals with a few exceptions. Once mixed, the liquid can be cooled and upon solidification the solid-state alloy is formed[12]. Alternative ways to make alloys include the use of solutions containing the components as salt[15], electrolysis[16], or simultaneous reduction of oxides of the components[17].

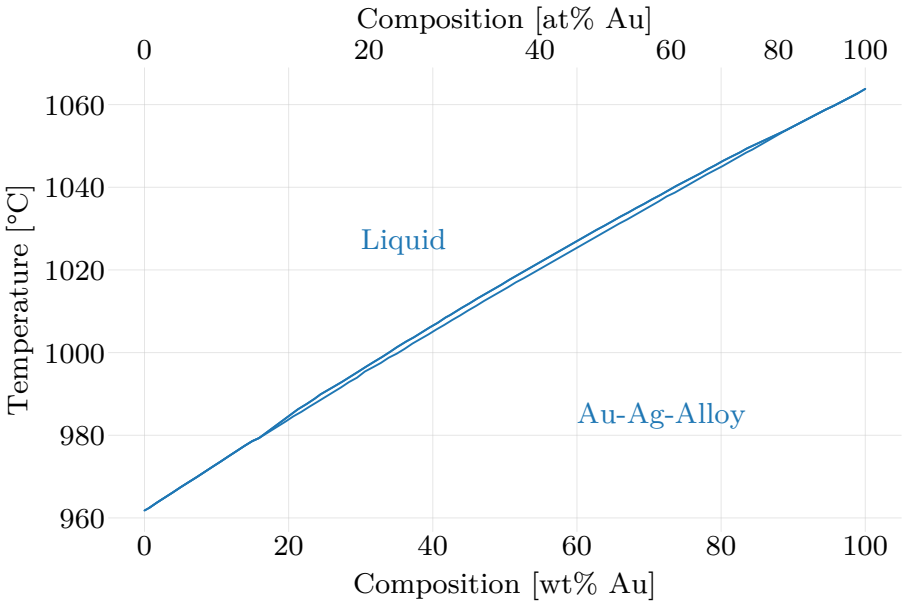

Figure 2.3: Phase diagram of silver-gold. For the largest part of the diagram it forms either a random alloy in the solid state (below the solidus line) or is mixed in liquid phase. In the small area between the liquidus and solidus lines a liquid and solid phase exist simultaneously. The data are from Okamoto et al.[12]

At the nanoscale, additional effective ways to make alloy nanoparticles are via colloidal synthesis[18] or via thermal annealing of layered thin films[19]. The route of thermal annealing was used in **Paper I** and **Paper II**, by nanofabricating layered nanoparticles comprised of metal A and B by means of nanolithography (see chapter 5)[20]. During the high temperature treatment, the system reduces the Gibbs free energy by eliminating the concentration gradient of metal A and B via atomic diffusion in the solid state, resulting in a homogeneous concentration in the end of the process. This behavior can be described with *Fick's law of diffusion*[21].

2.2 Segregation

Segregation describes a phase separation process in alloys driven by de-mixing for instance at a surface due to local energetics that are different than in the bulk of the crystal[22]. Such segregation can appear in different forms. For example, den-

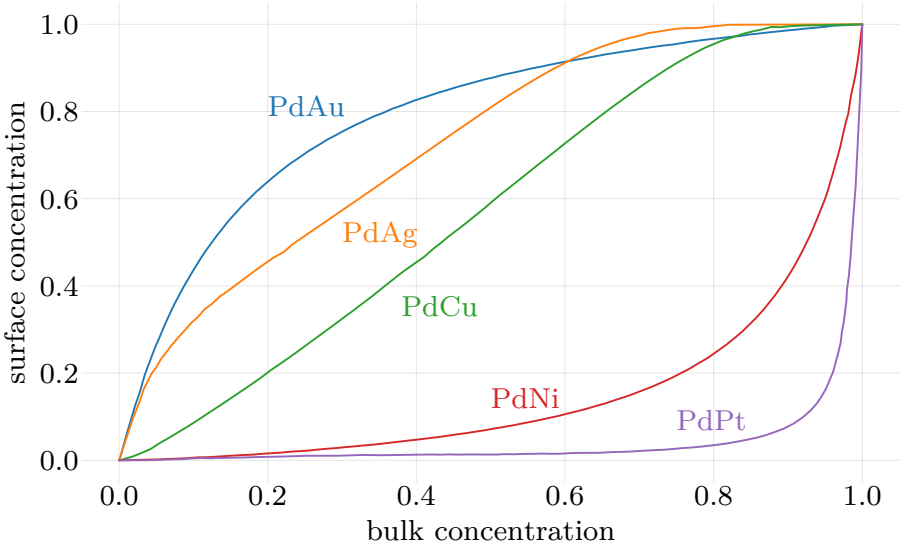

Figure 2.4: Calculated surface segregation for different palladium alloys for the (1 1 1) plane in vacuum at 600 K. Depending on the composition and the constituents, the surface concentration differs considerably from the bulk composition. Common reasons driving the segregation are the enthalpy of mixing, surface energy, size mismatch of the atoms, or also the gas environment. The shown concentrations are in respect to the element alloyed with Pd. The data are from Zhao et al.[22]

drites may form inside the material and thereby creating regions in the bulk material with an altered composition[23]. Alternatively, one can get segregation due to an inhomogeneous freezing process upon solidification[23] and many more. For my work presented in this thesis, equilibrium segregation at the surface of an alloy is most important. To this end, theory predicts for noble/transition metal alloys, that the surface composition is expected to – sometimes dramatically - differ from the bulk composition. This is exemplified for different palladium alloys in Figure 2.4. Common reasons driving the segregation are the enthalpy of mixing, surface energy, size mismatch of the atoms, or also the gas environment[22].

An estimate of which alloy that will exhibit significant surface segregation in vacuum or inert atmospheres can be obtained by looking at the surface energies of the constituents since the alloyed system tries to attain a state of lowest energy. Therefore, the element with a lower surface energy will segregate to the surface and the driving force for this process will be larger, the larger the difference in surface energy between

the alloy constituents. For Palladium the surface energy is $2.05\,\mathrm{J/m^2}$ and for gold $1.5\,\mathrm{J/m^2}$ [24]. Hence, as can be seen in Figure 2.4, gold is expected to segregate to the surface in vacuum. Nickel on the other hand has a higher surface energy than palladium with $2.45\,\mathrm{J/m^2}$ [24] and therefore palladium is segregating to the surface. Importantly, however, most of the time these materials are not used in vacuum but under high pressure conditions, such as during a catalytic reaction. Under these conditions physi- and chemisorption of atomic and molecular species on the surface play an important role and will alter the segregation behavior of the alloy. In most cases, if one of the gas atoms or molecules interacts strongly with one of the alloy constituents, it will tend to enrich on the surface[25] and create a surface composition not present in vacuum. However, cases have been reported were the less reactive constituent of the alloy is pulled to the surface[26].

3 Dielectric Functions and Plasmonics

3.1 Plasmons

To understand plasmons it is best to start by looking at the behavior of metals when they interact with electromagnetic radiation. One way to do this is by using the free-electron-gas model. It describes metals as free moving electrons with a fixed positive ion background. The model sometimes is also called the plasma model[27].

The driving force to excite plasmons is the external electric field, $\mathbf{E}$, which can be expressed as a harmonic wave $\mathbf{E}(t) = \mathbf{E}_0 e^{i\omega t}$. The resulting motion of the electrons is a classical harmonic oscillator and can therefore be written as[27]

$$m\ddot{\mathbf{x}} + m\gamma\dot{\mathbf{x}} = -e\mathbf{E}\,. \tag{3.1}$$

Here γ is the characteristic collision frequency, $\gamma = 1/\tau$, and τ is the relaxation time. Further we have the effective mass, m, of an electron and the elementary charge e.

A solution to Equation 3.1 is[27]

$$\mathbf{x}(t) = \frac{e}{m(\omega^2 + i\gamma\omega)}\mathbf{E}(t)\,. \tag{3.2}$$

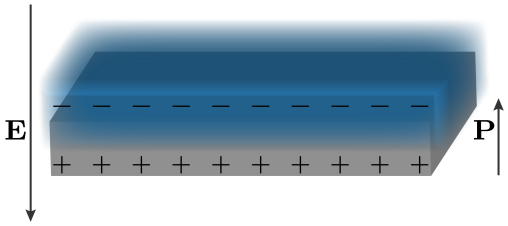

Figure 3.1: Volume plasmon in a slab of metal. The displacement of the electrons due to the electric field **E** creates the polarisation **P**.

Which leads with the polarization $\mathbf{P} = ne\mathbf{x}$ to

$$\mathbf{P} = \frac{-ne}{m(\omega^2 + i\gamma\omega)}\mathbf{E}\,. \tag{3.3}$$

The displacement of the electron cloud can be illustrated as shown in Figure 3.1.

The dielectric displacement, **D**, from Maxwell's equations is defined as

$$\mathbf{D} = \epsilon_0\mathbf{E} + \mathbf{P}\,, \tag{3.4}$$

which gives us

$$\mathbf{D} = \epsilon_0\mathbf{E} - \frac{-ne}{m(\omega^2 + i\gamma\omega)}\mathbf{E} \tag{3.5}$$

$$\mathbf{D} = \epsilon_0\left(1 - \frac{\omega_P^2}{\omega^2 + i\gamma\omega}\right)\mathbf{E} = \epsilon_0\epsilon\mathbf{E}\,. \tag{3.6}$$

ω_P is the so-called plasma frequency with $\omega_P = \frac{ne^2}{\epsilon_0 m}$. One can also see that in Equation 3.6 the complex dielectric function

$$\epsilon(\omega) = 1 - \frac{\omega_p^2}{\omega^2 + i\gamma\omega} \tag{3.7}$$

appears. The complex dielectric function can be written with its real and imaginary part separated

$$\epsilon(\omega) = \epsilon_r(\omega) + i\epsilon_i(\omega) \tag{3.8}$$

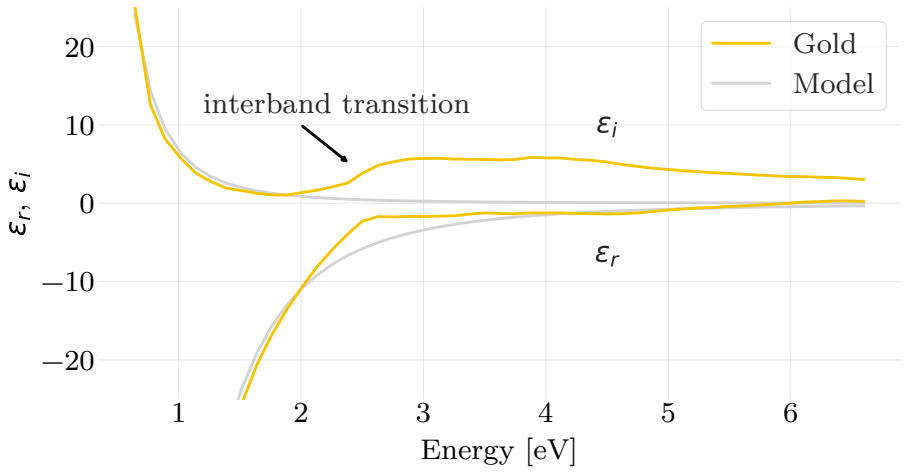

Figure 3.2: The dielectric function of gold from Johnson and Christy[28]. In grey the Drude model is fitted to the data. One can see that the overall agreement for the real part is good. However, the model description of the imaginary part works only until the onset of the interband transitions in Au. Adapted from Maier[27].

where the parts are

$$\epsilon_r(\omega) = 1 - \frac{\omega_p^2 \tau^2}{1 + \omega^2 \tau^2} \tag{3.9}$$

$$\epsilon_i(\omega) = \frac{\omega_p^2}{\omega(1 + \omega^2 \tau^2)} \tag{3.10}$$

Despite its ability to rationalize the core concept, a simple model as introduced above also comes with limitations, which can be seen in Figure 3.2. It shows the dielectric function of gold experimentally obtained by Johnson and Christy[28] and the dielectric function of Au obtained using the free-electron-gas model (Equation 3.7) fitted to the experimental data. At around 2.5 eV a strong deviation can be seen. At this point photons can with a high efficiency excite interband transitions between the 5d and the 6sp-band above the Fermi level[29,30]. This is an effect that is not included in the free-electron-gas model, as it treats mainly the sp-band.

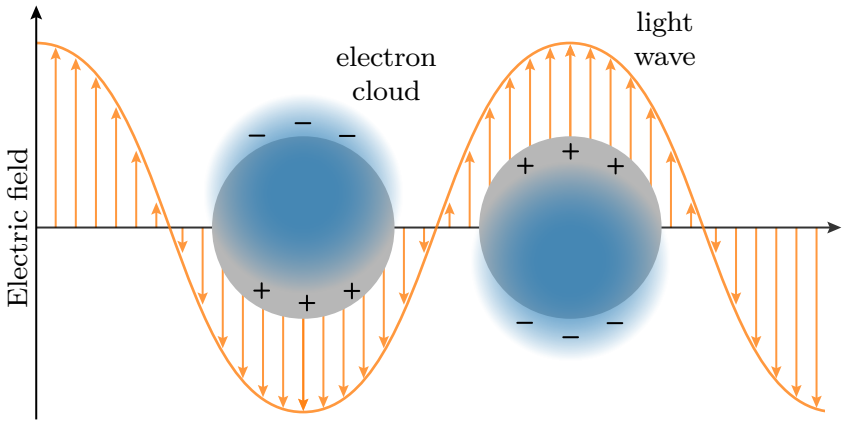

Figure 3.3: The free electrons of the nanoparticle are displaced by the electric field of the light and start oscillating. This is the classical picture of a localized surface plasmon resonance.

3.2 Localized Surface Plasmon Resonance

In the section above, we have seen that plasmons are the collective oscillation of the conduction electrons in metals. The displacement of the electrons is generated by an external electric field and the positively charged atom cores cause the restoring force. Due to the two counteracting forces one gets an oscillation. These oscillations do not only occur in bulk but can also be confined to a surface and either constitute a propagating or standing wave, which then are called surface plasmons or surface plasmon polaritons (SPP). If the plasmon is confined in a nanoparticle it is called localized surface plasmon (LSP) (Figure 3.3). The latter happens if the particle size is smaller than the wavelength, λ, of the external electric field and can conveniently be described by the *quasi-static approximation*[27]. This model has as its core assumption that, because the particle is much smaller than the wavelength, it can be treated as exposed to a static electric field. Based on the Laplace equation $\nabla^2\Phi = 0$, which can be used to describe the electric field $\mathbf{E} = -\nabla\Phi$, one can introduce the dipole moment, $\mathbf{p}$, at the center of the particle (for a more detailed derivation see Maier[27]), which reads as

$$\mathbf{p} = 4\pi\epsilon_0\epsilon_m a^3 \frac{\epsilon - \epsilon_m}{\epsilon + 2\epsilon_m}\mathbf{E}_0\,. \tag{3.11}$$

Where ϵ_m is the dielectric constant of the surrounding medium and a the radius of the particle. Similar to the dielectric function in the section above, one can then introduce a polarizability, α, via[27]

$$\mathbf{p} = \epsilon_0 \epsilon_m \alpha \mathbf{E}_0 \,, \tag{3.12}$$

which gives us

$$\alpha = 4\pi a^3 \frac{\epsilon - \epsilon_m}{\epsilon + 2\epsilon_m} \,. \tag{3.13}$$

From this expression it is easy to see that the polarizability experiences a maximum if the denominator reaches zero.

$$\mathrm{Re}\{\epsilon(\omega)\} = -2\epsilon_m \tag{3.14}$$

This is also called the *Fröhlich condition*.

From Equation 3.11 one can obtain the scattering, σ_{scat}, and absorption, σ_{abs}, cross sections as (see Bohren and Huffman[31] for details)

$$\sigma_{scat} = \frac{k^4}{6\pi}|\alpha|^2 = \frac{8\pi}{3} k^4 a^6 \left| \frac{\epsilon - \epsilon_m}{\epsilon + 2\epsilon_m} \right|^2 \tag{3.15}$$

$$\sigma_{abs} = k\,\mathrm{Im}\{\alpha\} = 4\pi k a^3\,\mathrm{Im}\left\{ \frac{\epsilon - \epsilon_m}{\epsilon + 2\epsilon_m} \right\}. \tag{3.16}$$

For the sake of completeness and because it is the value most often measured experimentally, also the extinction cross section shall be mentioned here. It is obtained by the combination of Equation 3.15 and 3.16.

$$\sigma_{ext} = \sigma_{abs} + \sigma_{scat} \tag{3.17}$$

$$\sigma_{ext} = 9\frac{\omega}{c}\epsilon_m^{3/2} V \frac{\epsilon_i}{[\epsilon_r + 2\epsilon_m]^2 + \epsilon_i^2} \tag{3.18}$$

Here we can see again that the cross sections are maximized when the Fröhlich condition is met. At this point, we also note that, the particles have a larger optical cross section than their geometrical cross section, which means they interact a lot more strongly with light than just casting a shadow[27].

It is further interesting to notice that scattering and absorption scale differently with nanoparticle size. Absorption dominates due to the a^3 scaling (Equation 3.16) in the small particle regime ($a \ll \lambda$)[27], while scattering dominates for larger particles due to the a^6 scaling (Equation 3.15).

3.3 Finite Difference Time Domain Electrodynamic Simulations

The Finite Difference Time Domain (FDTD) method is a numerical computational technique to simulate electrodynamics and calculate, for example, the LSPR of nanoparticles and nanostructures. As opposed to *Mie* or *Gans* analytical theory[27,31], using FDTD one is not limited to idealized shapes like spheres and spheroids. FDTD works by solving Maxwell's equations. They are solved in the time domain, which has the advantage that with a single run one gets a broadband result and not just one frequency. The finite difference in FDTD comes from the finite-difference approximation for the derivative[32]

$$\frac{df_{1.5}}{dx} = \frac{f_2 - f_1}{\Delta x}\,, \tag{3.19}$$

which means that finite steps in time are used. However, not only time is in finite steps, also the space is divided into finite steps, the so-called grid. If one looks at Maxwell's differential equation, one can see that the electric field depends on the change in the magnetic field (the curl) and vice versa. Calculating this curl in multiple dimensions becomes complex. To avert this, the electric and magnetic field components are staggered in space. Each electric field component ends up between magnetic field components in the grid and vice versa. For each grid space Maxwell's equations can now be solved. This concept was introduced in 1966 by Kane Yee[33] and is therefore called Yee grid.

FDTD has the advantage that it is an accurate, robust and mature method, which has been used very successfully for decades. The numerical complexity further scales just linearly with the problem size[32] and it is easy to parallelize, and therefore use the advantage of modern computers CPU architecture[34].

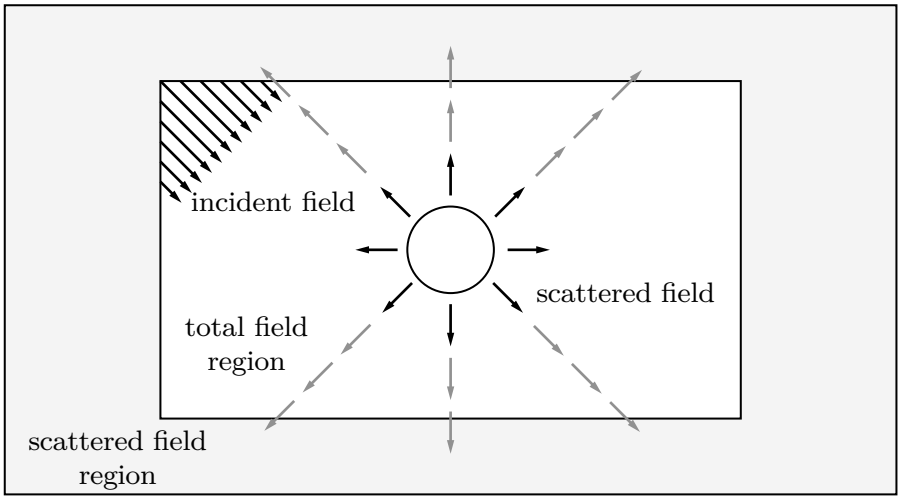

Figure 3.4: An example of a total field scattered field (TFSF) light source typically used in FDTD. In the total field region (black) both an incident and scattered (grey) field exist. In the scattered region, only scattered light is present. This eliminates backwards propagating energy and therefore 100% of the injected energy is incident on the simulated device object.

To simulate an incoming plane wave, a source that is often used in FDTD is the so-called total field scattered field (TFSF) source (Figure 3.4). With this source, the simulation is divided into different regions. The total field includes the incident and scattered fields together and then there are regions which only include the scattered field. This eliminates backwards propagating energy and therefore 100% of the injected energy is incident on the simulated object[32].

In this work, a single nanodisk was used in my simulations of the plasmonic response of nanoparticles investigated in the experiments. However, I want to stress that, in the experiments, the optical properties of the nanoparticles were measured from an array of nanodisks rather than from a single one. This may be problematic since, a priori, the optical response from an array is not identical to that of a single disk due to, for example, both near- and far-field coupling within the array[35]. However, since simulating arrays of nanoparticles is computationally more demanding, it is a commonly used approximation. In my case, where the experimentally studied arrays were made by Hole-Mask Colloidal Lithography (see chapter 5), they lack long-range order and the average particle-particle distance is about 2 -3 particle diameters. For such arrays, it has been shown[36] that the spectral position and full-width-at-half-

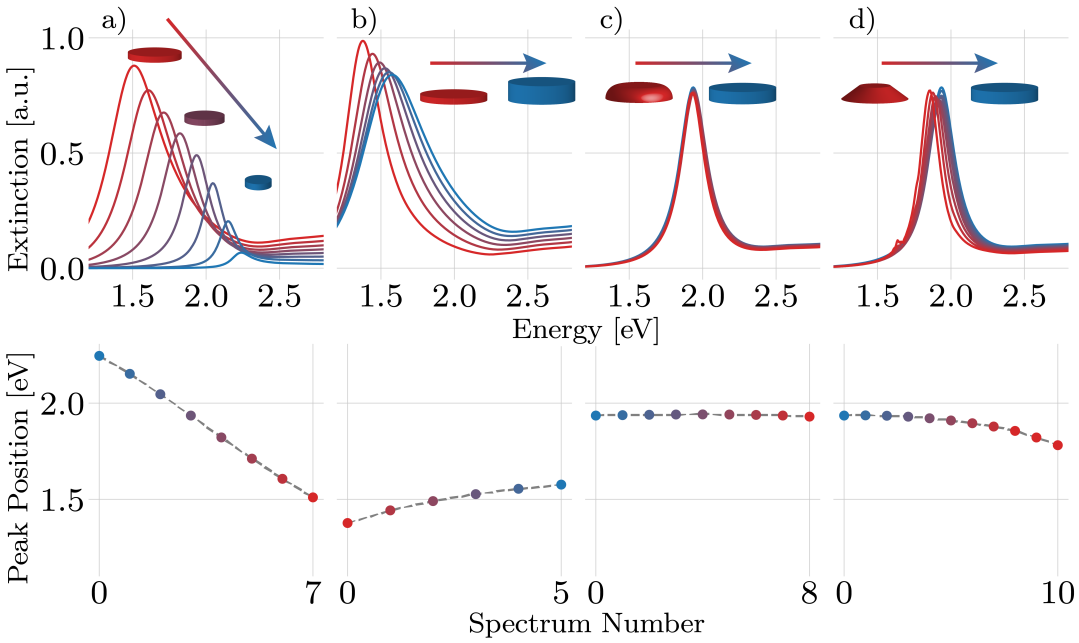

Figure 3.5: An overview of how different geometric features influence the LSPR of metal nanoparticles. The changes in disk a) diameter, b) height, c) top rounding radius, and d) tapering result in a different LSPR response. The bottom panels present the peak position as a function of the magnitude in geometric change, which demonstrates their different impact on the peak position. The calculation was done on a SiO_2 substrate with a refractive index of 1.46[37] and the dielectric function for gold from Rahm et al.[38] (**Paper I**).

maximum of the LSPR peak oscillates around the value of a single particle, with the specific values depending on the center-to-center distance of the particles in the array.

As mentioned above, it is not only the nature of an array that it is important for the optical response of plasmonic metal nanoparticles, but also the geometry of the individual nanostructures. To study individual nanostructures, FDTD is very suitable since it essentially enables the simulation of any shape. Therefore, I show some examples in Figure 3.5 to give an overview of how different geometric features influence the LSPR of metal nanoparticles, and I use the same geometrical features of a nanodisk that I used in the model in **Paper I**. Specifically, by reducing the diameter, the resonance frequency blueshifts as can be seen in Figure 3.5a. This is exactly the

behavior we expect by comparing it to spheres (see Equation 3.16). Also shown in Figure 3.5 is the influence of changing the nanodisk height b), the top rounding c) and the angle of the tapering d). One can see by looking at the lower half of the figure, where I plot the spectral position of the peak maximum as a function of geometry change (expressed as spectrum number), that changing the diameter of the disk yields the biggest spectral shift in resonance frequency.

3.4 Dielectric Functions of Transition Metal Alloys

As discussed in the previous chapter, when computing the plasmonic properties of metal nanoparticles using electrodynamics simulations, such as FDTD, the complex dielectric function of the metal is a required input. For pure metals this information is readily available from the literature, both derived in experiments and by first principles calculations[39,28,37,40,41].

Figure 3.6 depicts the dielectric functions of gold[28], silver[28], and palladium[37] and the corresponding LSPR calculated by FDTD for a single disk. Silver exhibits a peak at higher energies because the real part of the dielectric function is lower and shifted to higher energies compared to gold. Comparing silver with palladium, it is clear that the imaginary part of the dielectric function does not have a peak as clear as gold or silver. This is because the d-band for palladium is partially filled and intersects the Fermi level, whereas silver and gold have completely filled d-bands. The character of the electronic structure of palladium differs therefore compared to gold and silver, which can also be seen in the LSPR peak that is not as strong and broader compared to gold and silver. The width of the peak contains, further, information on the lifetime of the plasmon. A short plasmon lifetime is the result of a high damping factor as reflected by the imaginary part of the dielectric function. A big contribution to the damping factor for 140 nm nanoparticles of silver, gold, and palladium in the shown energy range is damping due to interband transitions[42]. Silver and gold both have a filled d-band well below the Fermi level (Figure 3.7), which leads to interband damping above a certain threshold, as can be seen in Figure 3.6a, whereas interband transition over the whole shown energy range dominate for palladium. In this case,

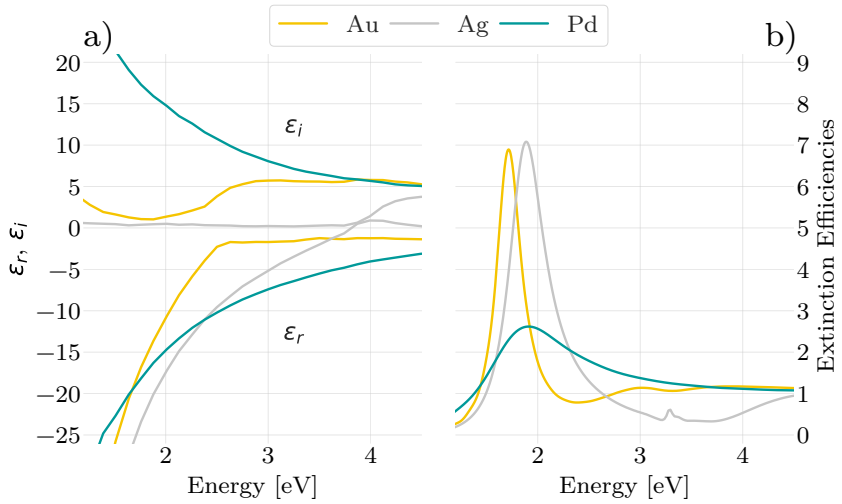

Figure 3.6: a) The dielectric functions of gold[28], silver[28], and palladium[28]. The imaginary part of gold and silver features a sudden rise at around 2.5 eV and 4 eV, respectively, where photons can with a high efficiency excite interband transitions. In the case of palladium the d-band is only partially filled and intersects the Fermi level. Therefore, interband transitions dominate over the whole energy range and lead to a higher imaginary part than gold and silver. b) The corresponding LSPR response calculated by FDTD using the dielectric functions above as input. Silver and gold feature a narrow and clear peak, whereas the palladium peak is not as strong and broader. The calculated response corresponds to a single nanodisk comprised of gold, silver and palladium with a diameter of 140 nm and a height of 25 nm on a fused silica support.

it can be concluded, that the plasmon lifetime for silver and gold is longer than for palladium.

The different electronic structure of the different metals makes it difficult to derive or predict the dielectric function for alloys from, for example, simple linear interpolation schemes. For systems where the electronic structure is similar, like gold-silver, one can use, for example, the modified Drude-Lorentz model[43], which works quite well (discussed in detail in section 3.5). In that case, we can see an almost linear shift of the d-band center (see Figure 3.7). If one, however, wants to generate a dielectric function for an alloy system where the constituent materials are of significantly different character in terms of their electronic structure, like, for example,

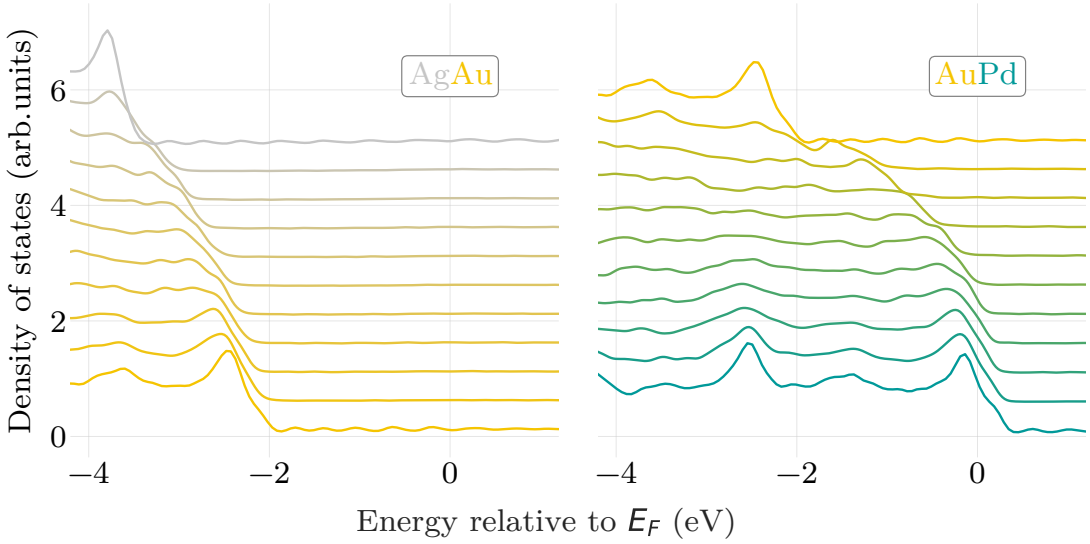

Figure 3.7: The electronic density of states of silver-gold and gold-palladium alloys with the mixing ratio changing in 10% steps, as calculated by DFT with van der Waals correlation[38]. In the case of silver-gold, which both have filled d-bands, an almost linear shift of the d-band center becomes apparent and it stays well under the Fermi level. In the case of gold-palladium, one combines two elements with open and closed d-bands, which already at low concentrations of palladium induces a strong non-linear shift of the d-band center.

gold-palladium, this simpler model is not applicable anymore. Specifically, in the case of gold-palladium, already a small amount of palladium shifts the d-band center in a non-linear fashion closer to the Fermi level (see Figure 3.7). This is the consequence of a hybridization of the Au $5d_{5/2}$ states and the Pd $4d$ states, and leads to a smearing of the Au $5d_{5/2}$ states[44]. For such systems more advanced first principles calculations like time-dependent density-functional theory have to be used, as we have done in **Paper I**.

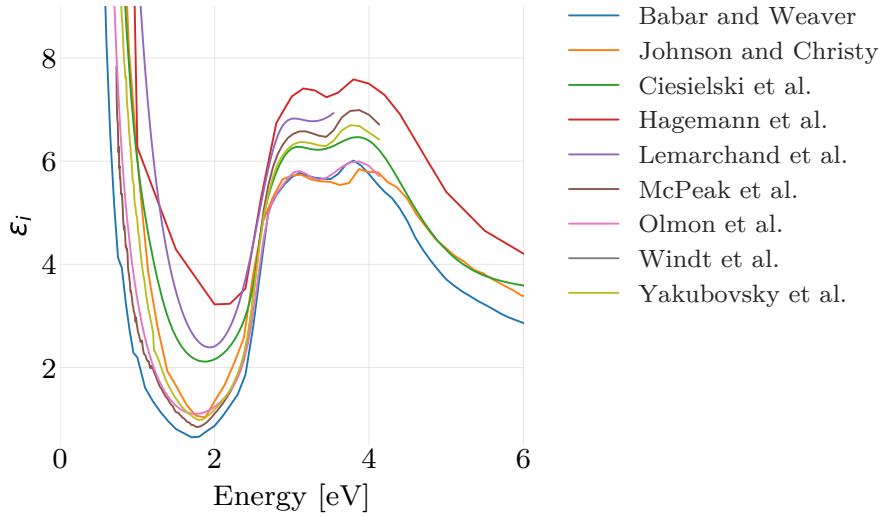

Figure 3.8: Experimentally measured imaginary parts of the dielectric function for gold collected from the literature. The overall shape of the curves is the same, but they are all different when comparing them in detail. The data are taken from Babar and Weaver[45], Johnson and Christy[28], Ciesielski et al.[46],Hagemann et al.[47], Lemarchand et al.[48], McPeak et al.[49],Olmon et al.[40],Windt et al.[50] and Yakubovsky et al.[51]

3.5 Optical Properties of Alloys

As discussed above, the optical properties of a solid can be described by the complex dielectric function

$$\epsilon(\omega) = \epsilon' + i\epsilon'' .$$

While straightforward in theory, it turns out to be experimentally challenging to accurately measure dielectric functions since features like surface roughness, morphology, surface oxidation, impurities and material thickness can dramatically affect the result[51]. Additionally, even processing parameters during film growth, and the used measurement technique have an influence on the outcome[52]. Figure 3.8 illustrates the effect of processing parameters and sample condition for pure gold. The overall trend is similar for all measured dielectric functions, but they differ in absolute values, especially in the region of the Drude peak, which ranges from almost 0 to around 3 eV. When it comes to alloys, the situation is no different and surface segregation and potential material inhomogeneities add further difficulties.

Therefore, reliable dielectric functions for alloy materials are very scarce in the literature.

For gold-silver alloys several attempts have been made to calculate, rather than measure, the dielectric function. The easiest way to do so is a weighted average of the dielectric functions of the components gold and silver. However, the corresponding results are questionable[43] since the model does not take into account that there is only one onset of the d-band. A more sophisticated approach was used by Gaudry et al.[53] in which a weighted average for the interband transition was used[53]. But even this approach neglects important physical change in the rest of the electronic structure and is not accurate enough. To increase the accuracy, a more complex analytical model was developed by Rioux et al.[43] and fitted to experimental data. The key point of this approach is that the actual joined density-of-states is modelled and forms the basis of the analytical model. This was the first time a model for calculating the dielectric function for gold-silver was based on the actual band-structure.

From the above discussion, it is clear that it is not trivial to obtain dielectric functions of alloys, even for the "easy" case of gold-silver, where the constituents have similar electronic structure, lattice constant, crystal structure and valences[43]. A second consequence of the above analysis of pursuit methods is that, if one is interested in the optical properties of different and/or more complex alloys, complete and consistent data sets for dielectric functions do not exist to date. One has to use either different experimental data sets, which are often small in terms of studied compositions or were only measured for a narrow spectral range, or one has to work with models that are (too) simplistic. This situation motivated the work presented in **Paper I**, where we introduce a library of transition metal alloy dielectric functions for the binary alloys of silver, gold, copper, palladium and platinum. To calculate the dielectric functions, we used linear response time-dependent density function theory (LR-TDDFT) with so-called special quasirandom structures, which can reproduce random alloys on a much smaller unit cell. This makes them an excellent choice for computational expensive techniques like LR-TDDFT[54]. The obtained dielectric functions are now freely available via a web application located at `https://sharc.materialsmodeling.org/alloy_dielectric_functions/`.

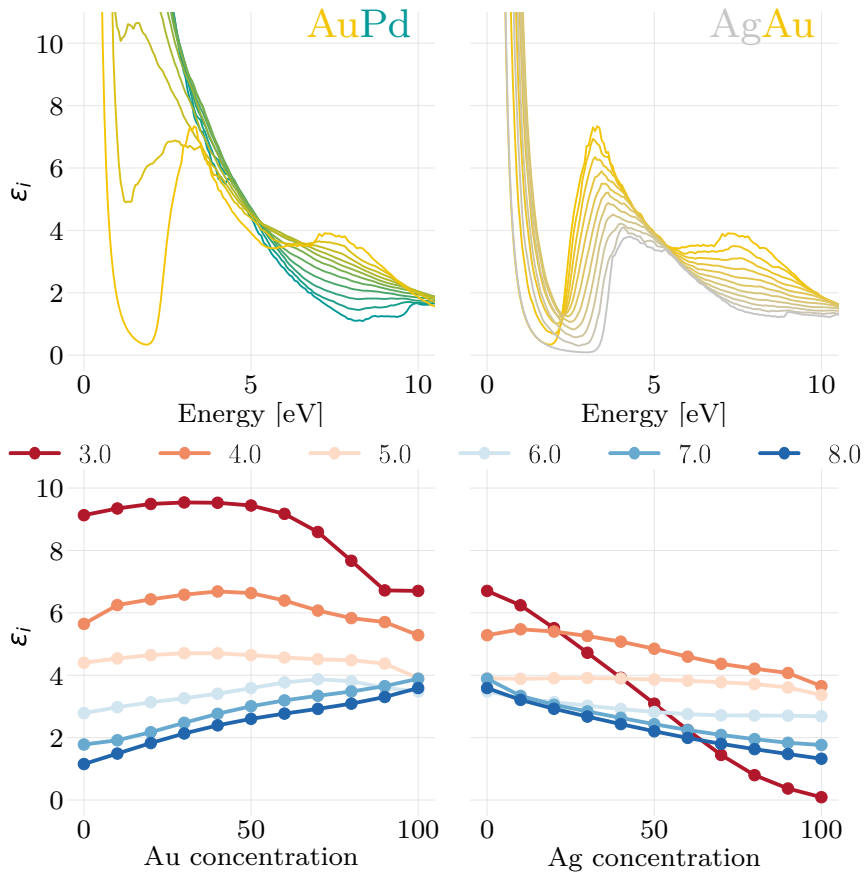

Figure 3.9: The dielectric functions of silver-gold and gold-palladium alloys as an example for isovalent and non-isovalent alloys obtained by TF-LRDFT by Rahm et al. (**Paper I**). The imaginary part is plotted versus the energy and versus the alloy composition for discrete energies, resulting in an energy cross section. The results show that the energy cross section in the low energy region for the non-isovalent alloys has a non-linear behavior.

From a physics perspective, the different alloys considered in **Paper I** can be divided into isovalent and non-isovalent systems, for example silver-gold (isovalent) and gold-palladium (non-isovalent), as depicted in Figure 3.9. As the key point, one can see that for the isovalent case the dielectric function changes linearly for all energies upon changing alloy composition, whereas for the non-isovalent case, especially in the low energy region up to around 4 eV, the dielectric function experiences a strong non-linear change. This clearly highlights that especially elements with different electronic

structure show interesting non-linear behavior in their optical response upon alloying. An effect not captured by more simple analytical models.

4 Catalysis

4.1 Heterogeneous Catalysis

Catalysis is one of the cornerstones of modern society. In this context, many people might only think of the three-way-catalyst in cars, but the technical relevance of catalysis goes far beyond this application. For example, nowadays 85% - 90% of the chemical industry uses a catalytic reaction somewhere in their processes[3]. Examples include refining of crude oils, and production of bulk and fine chemicals. Among other things, these are used in agriculture, polymers, pigments, pharmaceuticals and consumer products.

Mechanistically, catalysis is the change of rates of a chemical reaction with the help of a catalyst, which itself is not consumed by the process. The two main technical reasons why catalysts are very important is that they can increase the reaction rate towards the desired product (activity) and/or decrease the reaction rate towards an unwanted product (selectivity) of a reaction. One way of schematically depicting a catalytic reaction is with a so-called catalytic cycle (Figure 4.1). It shows the reaction pathway including a catalyst with multiple elementary steps. It also shows that the catalyst itself is not consumed during the reaction.

In catalysis, one normally differentiates between homogeneous and heterogeneous catalysis. In homogeneous catalysis the catalyst is in the same phase as the reactants. A famous example is the creation of the *ozone hole* in the 80s[3]. Here chlorine acted as catalyst and increased the rate of

$$O_3 + O \rightarrow 2O_2\,. \tag{4.1}$$

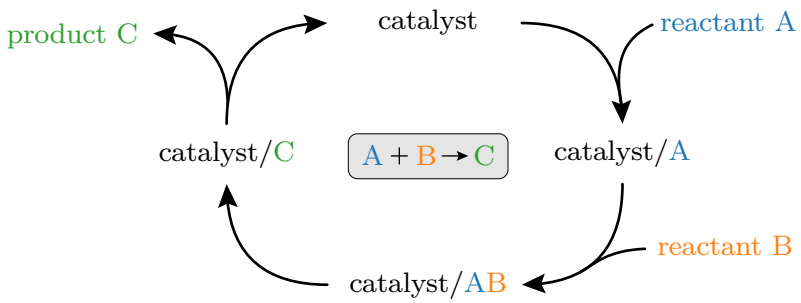

Figure 4.1: Schematic of a catalytic cycle forming the product C out of reactants A and B with help of a catalyst. The reaction occurs via multiple elementary steps and the catalyst itself will not be consumed during the reaction.

The focus of this thesis lies on heterogeneous catalysis, where the catalyst is in a different phase than the reactants and products, typically in the solid state, meaning the reactions occur on a surface. Heterogeneous catalysis is considered the work-horse of the chemical and petrochemical industry[3]. An example is the catalytic oxidation of carbon monoxide over noble metals like palladium, platinum or rhodium. It is used for example in car exhaust catalysts and will be discussed in more detail in section 4.3.

To illustrate how a catalyst works in general, it is also useful to have a look at the potential energy diagram of a reaction. In Figure 4.2 is this shown for the arbitrary reaction $A+B \rightarrow C$. It illustrates that the catalyst offers an alternative reaction pathway, normally with several steps that are energetically favorable compared to the uncatalysed reaction. To this end, it is also important to note that a catalyst only changes the kinetics of a reaction and not the thermodynamics[3].

A guiding principle in catalysis is the *Sabatier's principle*. It relates to the fact that if the interaction between catalyst and reactants is too weak, they will not bind to the catalyst and the catalytic reaction cannot happen. On the other hand, too strong reactant-catalyst interaction does not provide the reactant as the entire surface will be covered at all times, not leaving any free sites for the other reactant to bind and react. This phenomenon is known as poisoning. The same problem applies to the product. If it binds too strongly on the surface it will not desorb and not free active sites for the reaction to continue. This balance, and on which side a catalyst is located

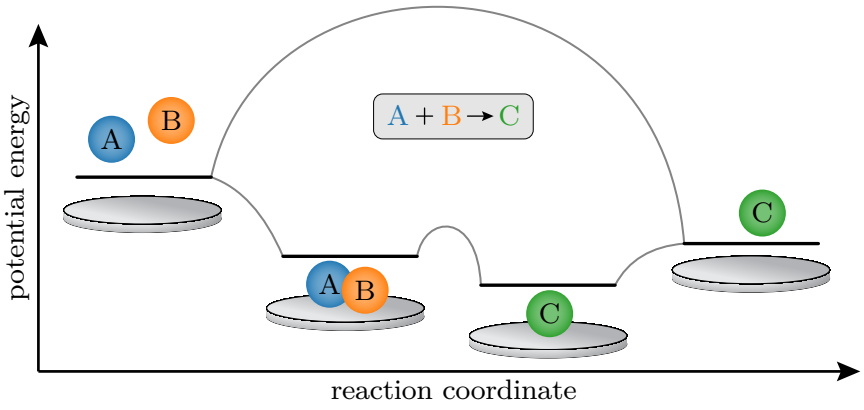

Figure 4.2: The potential energy diagram of a chemical reaction $A + B \rightarrow C$ in the presence and absence of a heterogeneous catalyst. By adding a catalyst, the potential energy landscape changes and allows for a different reaction pathway. Adapted from Chorkendorff and Niemantsverdriet[3].

for a specific reaction, can be depicted as a *volcano plot* as shown in Figure 4.3, where the ideal catalyst would be located at the top.

When it comes to catalyst materials, it is not just single elements that are used but also alloys are becoming increasingly important, as they become more and more available in nanoparticle form. In catalysis, alloying can be regarded as an additional handle for tailoring activity or selectivity of the catalyst. To give one example, gold-palladium alloys are used for the vinyl acetate synthesis, since they show superior activity compared to the classic monometallic catalyst palladium[56].

Mechanistically, there are two kinds of effects that alloying can impose on catalyst function[25]. The first is that due to the alloying the electronic structure of the catalyst changes. This means that chemical properties of the material and bond strengths of the adsorbates will change, and therefore the overall reactivity[57]. This effect is usually referred to as *Ligand effect*.

The second effect is the *ensemble* or *geometric effect*. Due to the alloying the amount of identical multiple surface absorption sites decreases and single-atom site abundance increases, which in turn modifies chemisorption and therefore the reaction properties of the adsorbates[25]. For example, catalytic reactions which require large assemblies of active sites will be effectively suppressed[57].

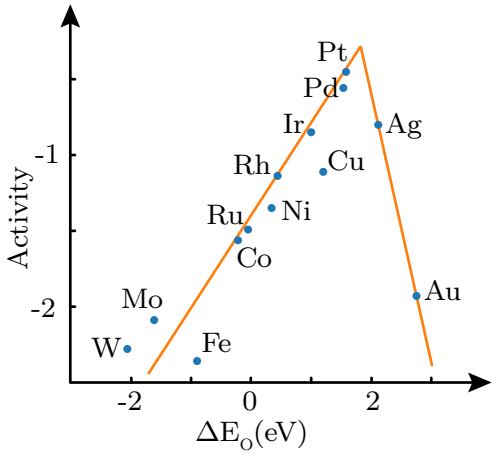

Figure 4.3: A classic Volcano plot showing the activity of the oxygen reduction reaction depending on the oxygen binding energy for different metal catalyst materials. To increase the oxygen reduction rate is an important step to improve low temperature fuel cells. Adapted from Nørskov et al.[55]

It should be highlighted that the composition on the surface of an alloy catalyst is seldomly equal to the bulk composition and may dynamically change during reaction (see section 2.2). Due to such effects, surface alloys can emerge that would not exist in bulk[58]. Because catalysis normally happens at elevated pressures other parameters than surface energy can be the controlling factor. If, for example, one of the components interacts strongly with one of the reactants, it could influence the surface composition of the alloy severely[22].

4.2 Plasmon Mediated Catalysis

Plasmon mediated catalysis is a sub area of photocatalysis, where metal plasmonic nanostructures are employed to capture light and concentrate the corresponding energy at the nanoscale, where it is anticipated to impact catalytic reactions[59,60]. For simplicity, I use the term “photocatalysis” below as a general term for plasmon mediated catalysis.

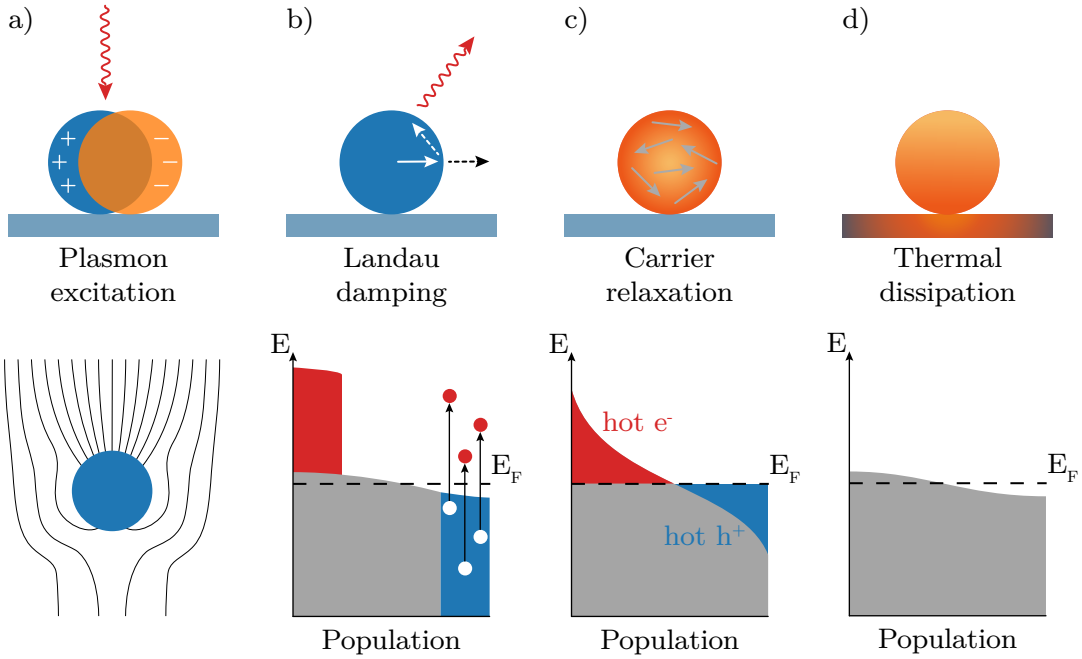

Figure 4.4: a) Initially, the LSPR is excited in a nanostructure by irradiating light at the resonance frequency. b) The plasmon can decay by either radiatively by re-emitting a photon or nonradiatively by Landau damping, which creates hot charge carriers. c) The hot carriers will relax and redistribute their energy via electron-electron scattering. d) The lower energy charge carriers can now interact with phonons and lead to increased temperature, which will also dissipate to the surroundings, such as the support. Adapted from Brongersma et al.[60]

The field is divided into two sub-areas, namely direct and indirect photocatalysis[59]. The indirect route refers to systems that combine plasmonic nanostructures with semiconductors. In this scheme, the LSPR captures energy from the light, which is then transferred to the semiconductor where the catalytic process occurs. A famous example is the plasmon-enhanced water splitting reaction on TiO_2 using plasmonic gold nanoparticles to produce hydrogen[61]. In contrast, in the direct scheme, the plasmonically active material acts as energy capturer and catalyst at the same time, as demonstrated in the seminal work by Christopher et al. for the ethylene epoxidation reaction over Ag nanocrystals[5].

To provide some understanding for the energy flow in a plasmonic nanostructure after

excitation of the LSPR, it is useful to discuss the involved processes. The first step is to excite the LSPR by irradiating light at the resonance frequency of the nanostructure at hand (Figure 4.4a). Once excited, the plasmon has two ways to decay, either radiatively by re-emitting a photon or nonradiatively by Landau damping[59]. Landau damping creates hot charge carriers (Figure 4.4b). The term "hot" indicates that the excitation energies are higher than the thermally exited equivalent at room temperature. The resulting energy distribution depends on particle size[62], plasmon energy and material (electronic structure)[63]. The time scale for Landau damping is below 100 fs[64]. After the hot carriers are created they will relax and redistribute their energy via electron-electron scattering (Figure 4.4c). This happens at a time scale of around 0.1 ps to 1 ps[60]. These lower energy electrons, sometimes called warm electrons, can now interact with phonons and lead to increased temperature, which will also dissipate to the surroundings, such as the support (Figure 4.4d). This happens in a range of 100 ps to 10 ns.

In principle, all these effects can contribute to catalysis by either increasing the rate or changing the selectivity of a reaction. The hot charge carriers can, for example, excite electronic or vibrational transitions in adsorbed molecules or can occupy a specific molecular orbital and induce desorption, dissociation or translational motion[60]. Mukherjee et al.[6] showed for example the dissociation of H_2 at room temperature over gold particles using a laser in the visible range. Here, the hot electron transfer from the gold nanoparticle into an antibonding orbital of the H_2 is believed to trigger the dissociation.

Alternatively, it has also been reported that the plasmonic field enhancement or the localized heating effect can help to drive the reaction[59]. To utilize field-enhancement, typically a plasmonic particle acts as an antenna and a catalytic particle is placed inside the near-field leading to increased activity of the catalyst[65]. A photochemical rate enhancement due to near-field enhancement is expected to be proportional to the rate of incident photons[66]. Temperature induced reaction rate enhancement works because chemical reactions, to be exact the rate constant, k, typically obey the Arrhenius equation

$$k = A \exp\left(\frac{-E_a}{RT}\right). \tag{4.2}$$

T is the temperature, E_a is the activation energy, R is the gas constant, and A is the pre-exponential factor.

Despite almost a decade since the first papers in the field were published, there is (still – or maybe even more of) a controversy about the dominant reaction enhancing mechanism in plasmon mediated catalysis[67]. This important discussion is essentially centered on the problem that it is very difficult to unambiguously distinguish between direct influence of the energetic charge carriers[6] and pure thermal effects[8]. In some cases, the findings can be explained either way, as was shown by Sivan et al.[8] and even more recently by Baffou et al.[66].

One of the core problems is that the *exact* temperature of the catalyst is very hard to determine. In fact, it is either not known or largely underestimated, as discussed by Sivan et al.[8]. This arises from the difficulty to precisely measure the temperature of the catalyst particles or even active sites since most techniques measure the *average* temperature of the sample. Another argument why direct hot-charge-carrier effects are probably less common than claimed is the very short life time of these carriers as is discussed above. It makes the probability of interaction with the surroundings very low[66].

4.3 CO Oxidation

Carbon monoxide is a toxic gas at concentrations above 200 ppm[68]. At the same time, it is not possible for humans to detect it because it is colorless, tasteless and odorless. The toxicity for humans and animals is based on COs ability to bind to haemoglobin. This reduces the ability of the blood to carry oxygen[69]. Depending on the concentrations and time of exposure it leads to headache, vomiting, dizziness, chest pain, passing out and death[70]. Due to the high toxicity of CO, the abatement and reduction of it is used in car-catalysts but also in respirators, for, for example, firefighters[71].

The main source of CO is the partial combustion of fuels. One to two percent of car's exhaust is carbon monoxide. Because we have a lot of cars in our society, they are the biggest producers of CO. In cities transport is responsible for up to 90 %[72]of

the CO emissions. To reduce the emission, today, three-way catalytic converters are found in essentially all gasoline vehicles.

Another area where CO abatement is important is in proton exchange membrane fuel cells (PEMFC)[73]. Specifically, it is critical to reduce the CO content of the hydrogen fuel to less than 50 ppm[72] since CO poisoning of the Pt catalyst otherwise dramatically reduces fuel cell efficiency.

To this end, there are 3 ways to remove CO from a gas stream: (i) absorption, (ii) methanation and (iii)catalytic oxidation[72]. Since catalytic oxidation of carbon monoxide to carbon dioxide is the most effective one, we will have a closer look at that. For the catalytic CO oxidation different catalysts are used. Noble metals like palladium, platinum or rhodium, which have high activity and have been used for a long time[74]. Due to the limited availability and the cost of noble metals, however, oxides of less scarce metals are of high interest, such as for instance Fe, Cu, Ni, Co[72,75,76]. Also explored are gold nanoparticles for low temperature CO oxidation[77]. Due to the low temperature capability they are often used in breathing apparatus and air purification[72]. The focus on this thesis is, however, CO oxidation on noble metals like palladium.

The catalytic CO oxidation on noble metals, such as platinum and palladium, is a classical example for *Langmuir–Hinshelwood* kinetics[3]. Here, all reactants first adsorb on the surface and then undergo a reaction and desorb from the surface (Figure 4.5)[3]. The corresponding elementary steps can be written as follows.

$$\mathrm{CO} + * \underset{k_1^-}{\overset{k_1^+}{\rightleftharpoons}} \mathrm{CO}* \tag{4.3}$$

$$\mathrm{O_2} + 2* \underset{k_2^-}{\overset{k_2^+}{\rightleftharpoons}} 2\,\mathrm{O}* \tag{4.4}$$

$$\mathrm{CO} * + \mathrm{O}* \underset{k_3^-}{\overset{k_3^+}{\rightleftharpoons}} \mathrm{CO_2} * + * \tag{4.5}$$

$$\mathrm{CO_2}* \underset{k_4^-}{\overset{k_4^+}{\rightleftharpoons}} \mathrm{CO_2} + * \tag{4.6}$$

The $*$ symbolizes free sites and $k^{+/-}$ represent the forward and back rate constants,

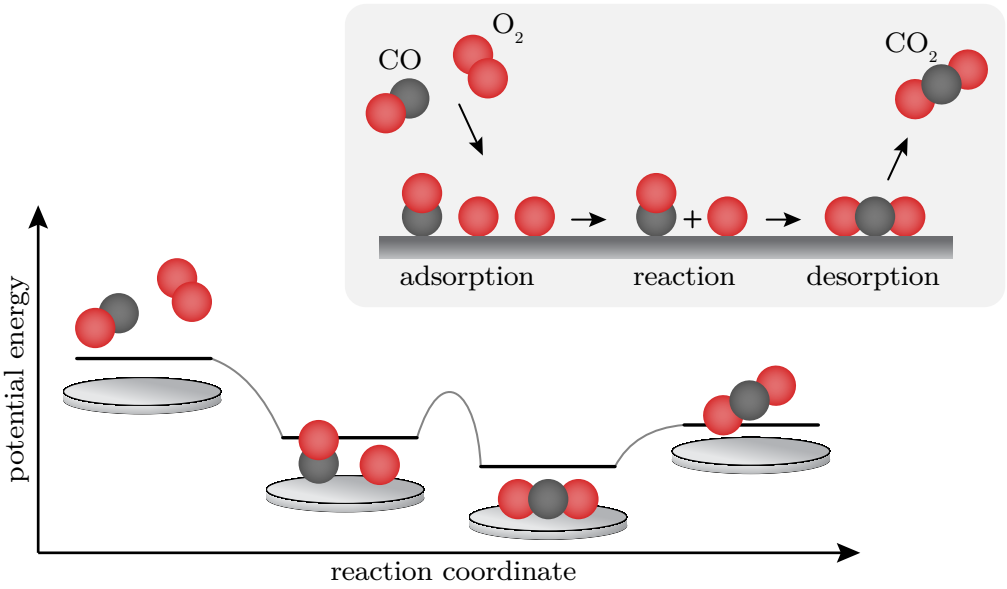

Figure 4.5: The reaction cycle and the potential energy diagram of CO oxidation. At first CO and O_2 are adsorbed on the catalyst surface and O_2 will be dissociated in the process. A single oxygen atom and a CO molecule will form a CO_2 molecule on the surface. The last step is for the CO_2 molecule to desorb. Adapted from Chorkendorff and Niemantsverdriet[3].

respectively. Step 4.5 is often considered to be the rate determining step (RDS). This is also depicted in Figure 4.5 because the energy barrier for this step is the highest among the forward reactions. Considering the RDS, the rate for the reaction follows as

$$r = k_3^+ \theta_{\mathrm{CO}} \theta_{\mathrm{O}} \,. \tag{4.7}$$

Here θ_x describes the coverage of CO and O_2 on the surface. The reaction rate can be plotted depending on the relative partial pressure, α, of CO and O_2 for constant temperature (Figure 4.6). It can be seen that at high O_2 pressure the surface is mostly covered with oxygen and only few CO molecules can adsorb and react, resulting in a low reaction rate. The surface is oxygen poisoned. Similarly, at high CO concentrations, reaction rate is low due to CO poisoning[3]. In the range between, the coverage of O and CO is more balanced and therefore reaction between them can occur. In this range the rate reaches its maximum. The shape of the rate curve is governed by the rate constants for CO and O_2 ad- and desorption and the formation

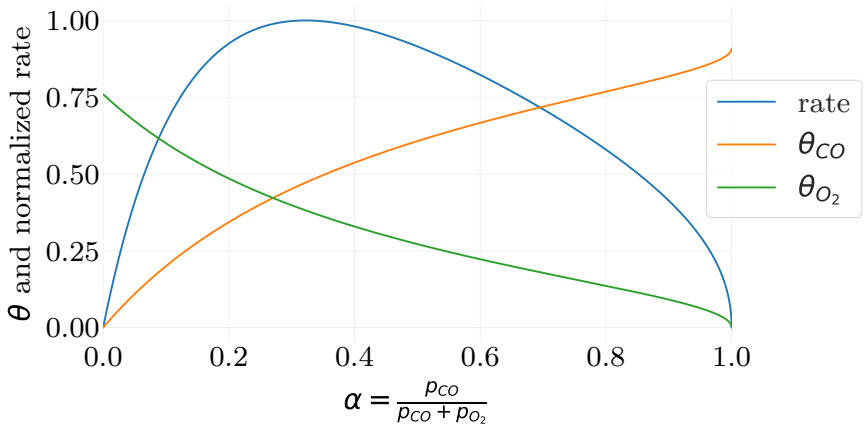

Figure 4.6: The calculated rate and surface coverage of CO and O_2 on a surface during CO oxidation for different CO and O_2 mixing rations α_{CO}. The rate constants for CO and O_2 ad- and desorption and CO_2 formation are chosen arbitrarily to be 10 and only serve the purpose to illustrate the behavior of a reaction following Langmuir-Hinshelwood kinetics. It can clearly be seen that the rate reaches a maximum and is reduced to the sides, where high relative concentrations of CO or O_2, respectively, cover the surface and poison it.

of CO_2. Thus, depending on total pressure, temperature, and catalyst material and state, the shape of the rate curve will change.

As already mentioned, classical catalysts with high activity for CO oxidation are the noble metals platinum, palladium and rhodium[72,78]. More recently also small gold nanoparticles were discovered to work for CO oxidation at low temperatures[77]. Therefore, the step to investigate gold-palladium alloys appears natural. However, even though palladium-gold alloys are an excellent catalyst for, for example, the hydrodesulfurization reaction[79] or the direct synthesis of hydrogen peroxide from H_2 and O_2[80] they are not very efficient for the conventional catalytic CO oxidation reaction[81].

The to date unexplored route of alloying plasmonic active gold with palladium in the context of plasmon-mediated catalysis is explored in **Paper II**. It is used to shine light on the discussion of the reaction enhancing mechanism when noble metal catalyst nanoparticles are irradiated with visible light during a catalytic reaction.

By alloying palladium with gold, we tailor the catalytic activity without radiation, while, at the same time, maintaining a constant optical cross-section. By comparing the neat palladium and alloy systems we show that the catalytic activity is not alone governed by the photon flux but also depends heavily on the temperature in the dark. A fact that commonly plays a minor role in the debate on enhancing mechanism in plasmon-mediated catalysis.

5 Nanofabrication

5.1 Hole–Mask Colloidal Lithography

All my samples were nanofabricated with a technique called *Hole–Mask Colloidal Lithography* (HCL)[82]. This technique offers the opportunity to make large area arrays of nano-objects like disks and dimers, as well as layered structures in terms of their composition. Furthermore, samples can be fabricated on a variety of surfaces, like fused silica, silicon or sapphire. The technique falls into the area of self-assembled nanofabrication, which has the advantage that it easily can produce nanostructures in the sub-100-nanometer range. At the same time the technique is scalable to large areas and comparably cost-effective[83].

The process for HCL is shown in Figure 5.1 and works as follows. After choosing a substrate (Figure 5.1a) it needs to be cleaned thoroughly. This is done by sonication in acetone and IPA (isopropyl alcohol). After cleaning, a thin PMMA (polymethyl methacrylate) sacrificial layer is spincoated onto the substrate (Figure 5.1b). After the spincoating the sample is plasma treated to increase the hydrophilicity of the PMMA. This makes it possible in the next step to dispense a polyelectrolyte solution of PDDA (Polydiallyldimethylammonium chloride) on the surface (Figure 5.1c). This creates a positively charged layer on top of the PMMA. Subsequently, a solution with negatively charged polystyrene (PS) beads is dispersed on the sample (Figure 5.1d). The PS beads, due to electrostatic interactions, are thereby assembling themselves on the surface in a quasi-random array without long-range order. The average center-to-center distance between particles can be tuned by screening the charge of the PS beads by adding small amounts of salt to the solution. After removing the excess beads by extensive rinsing in water and subsequent blow-drying a layer of chromium

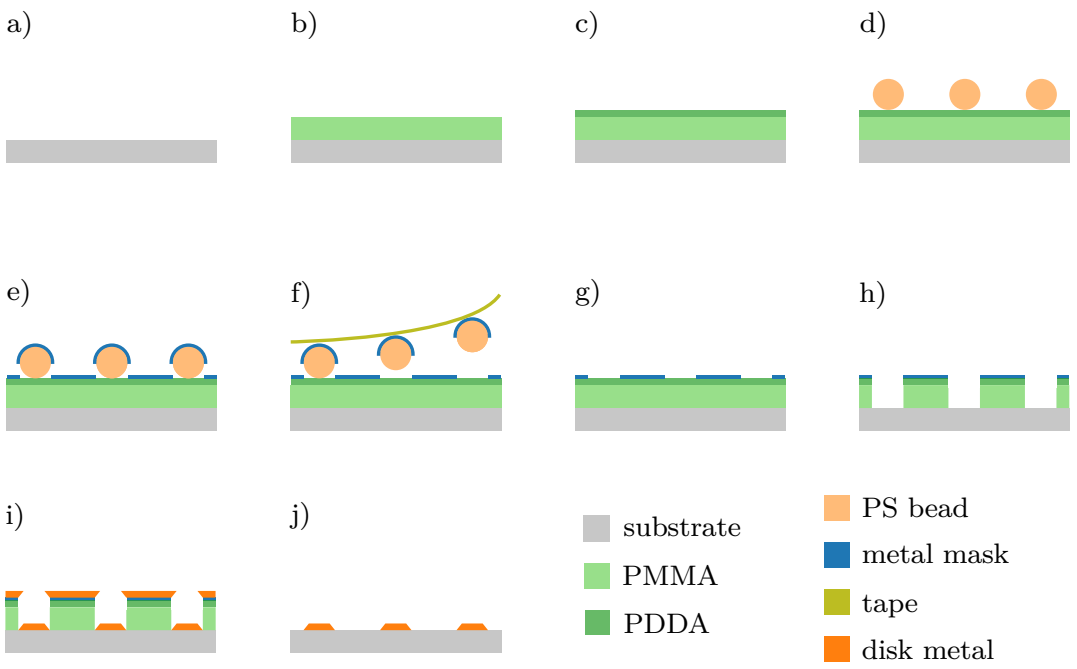

Figure 5.1: The process of creating a nanodisk array with hole–mask colloidal lithography. Using a) cleaned substrate, b) spin-coat PMMA, c) disperse PDDA, d) disperse PS, e) evaporate mask, f) tape-strip, g) holes in mask, h) plasma etching PMMA, i) evaporate metal, j) lift-off.

is evaporated onto the self-assembled PS beads (Figure 5.1e). After evaporation, the PS beads are removed by tape stripping (Figure 5.1f), which leaves holes with the diameter dictated by the PS beads in the Cr mask (Figure 5.1g). Then, by applying an oxygen plasma etch, the PMMA layer exposed through the holes can be etched away, leaving deep holes in the PMMA layer that extend all the way to the substrate (Figure 5.1h). After this step, the mask is ready to be used for evaporation of the metal (or other material) of choice. Depending on how the metal is deposited, one can create different nanostructures by using tilting and rotation of the substrate during evaporation[84]. To create nanodisks, as I have used in my work, the metal has to be deposited at normal incidence (Figure 5.1i). Different ways to deposit material through the mask will be discussed in the next section. The last step is the lift-off process (Figure 5.1j). Here acetone is used to dissolve the underlying PMMA layer to remove the mask. As the last step, the sample is rinsed with IPA and blow dried with N_2.

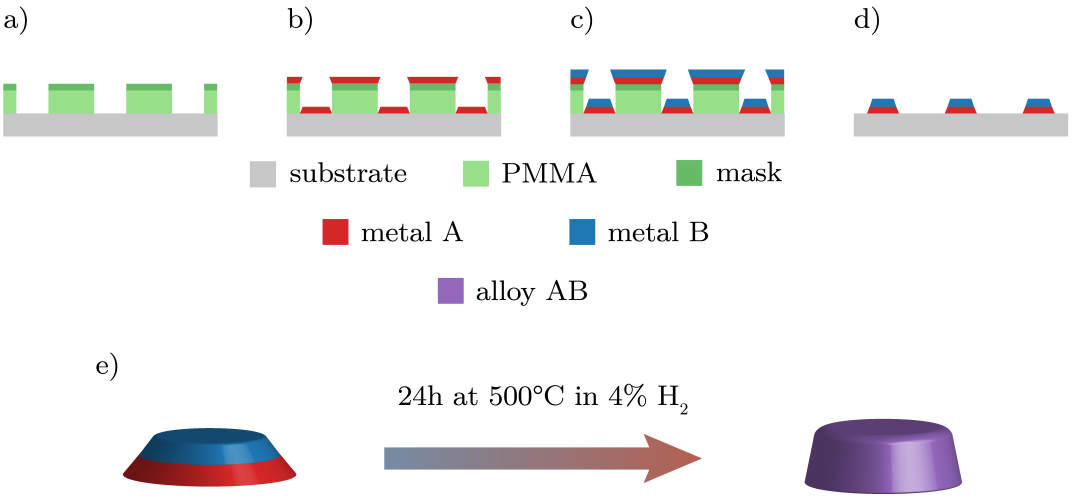

Figure 5.2: The process of creating an alloy nanodisk. The method uses a) a HCL created mask. b) Through the mask metal A is evaporated and c) subsequently the second metal B. d) During the lift-off the mask is removed and leaves behind the bare layered metal particles on the substrate. e) To create the alloy, the layered structures will be annealed at 500 °C to provide the needed atomic mobility to induce alloy formation in the solid state. During this process the nanoparticles will slightly change their dimensions and shape, with the specific depending on the metal-substrate interaction.

5.2 Material Deposition

The mask can be used to create single material or alloy structures of different type. For alloys the two alloy constituents are consecutively evaporated through the mask.

Technically, there is a large number of ways to grow a thin film on a surface. In general, thin film deposition methods can be divided into two categories, physical and chemical deposition. Chemical processes include for example wet-chemical methods or chemical vapor deposition, like atomic layer deposition. Physical processes on the other hand do not rely on a chemical reaction to form the thin solid film. Instead, they use means such as thermal evaporation or sputtering. Evaporation methods rely on the concept of evaporating a solid material by heating it to very high temperature

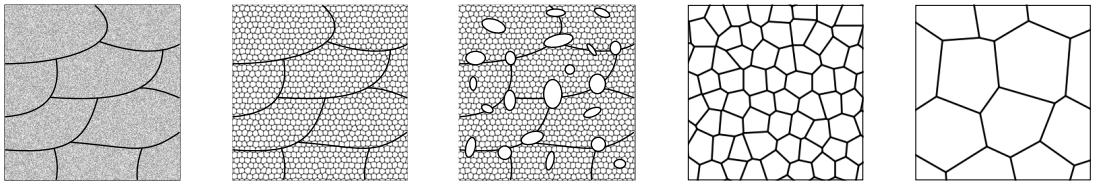

Figure 5.3: Schematic illustration of the steps recovery, recrystallization and grain growth during annealing. Adopted from Raabe[23].

and the vapor then condensing on the substrate where it nucleates and grows into a thin film. For these techniques, an ultra-high vacuum (UHV) is needed to create the necessary mean free path for the vapor to reach the substrate. The evaporation itself can be induced by various means. The target material can for example be heated with a high-voltage electron beam that is rastered over a source material (electron beam evaporation) or lasers can be used to heat the material (laser beam evaporation).

The process of nanofabricating alloy nanodisks uses a mask created by HCL (Figure 5.2a). Through the mask the first metal is evaporated (Figure 5.2b) and subsequently the second metal (Figure 5.2c), where the respective thickness of these two layers dictates the composition of the alloy. For all alloy nanofabrication in **Paper I** and **Paper II** I used electron-beam evaporation of the constituent metals. The last step is the lift-off process (Figure 5.2d), which then yields layered nanodisks on the substrate. To create, from this layered structure, a random alloy, one needs to anneal the system, which was done at 500 °C for 24h in 4% H_2.

5.3 Annealing

The last step in the nanofabrication of alloy nanoparticles is annealing. In fact, this can be an important step not only when nanofabricating alloys but also when targeting single element nanoparticles to, for example, control their morphology[85]. In case of the alloy nanostructures at hand, it is necessary to provide the needed

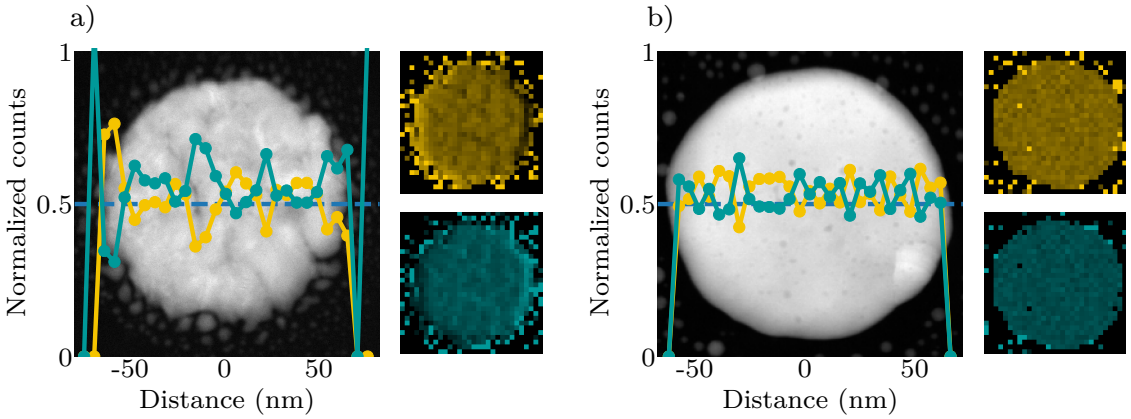

Figure 5.4: A high-angle annular dark field scanning transmission electron microscopy (HAADF-STEM) image of a a) unannealed and a b) annealed gold-palladium particle. The corresponding energy dispersive X-ray spectroscopy (EDX) images show the lateral distribution of gold (yellow) and palladium (green). The HAADS-STEM images reveal a strong reduction of grains during the annealing process. The line scan further confirms the homogeneous distribution of both elements across the particle after annealing. Data of annealed particles taken from Rahm et al.[38]

atomic mobility to induce alloy formation from the layered constituents in the solid state (Figure 5.2).

From a classical metallurgy perspective, the annealing process can be divided into 3 major steps : (i) recovery, (ii) recrystallisation and (iii) grain growth (Figure 5.3)[23]. During the first recovery step, dislocations and other defects show minor movement and rearrangement. This slightly decreases their density and more importantly it reduces the associated stress in the material[23]. Recrystallisation happens if the temperature reaches around 1/3 to 1/2 of the melting point of the material[23]. During this phase, new and strain free grain boundaries are formed, and high angle grain boundaries are reduced. Also, the defect density reduces drastically. The last stage is the grain growth where the new grains with low angle grain boundaries formed during the recrystallization step continue to grow, thereby reducing the overall grain boundary length and thus the free energy of the system[23]. Projected onto my nanodisk structures, given enough time and high enough temperature, they will transform into a single crystal (Figure 5.4).

6 Setup/Characterization

In this chapter I will describe the setup I used for the catalysis measurements included in **Paper II**. Furthermore, I will explain the different materials characterization techniques that were used to characterize the samples.

6.1 Catalytic Flow Reactor Measurement Setup

The setup for the catalysis experiments is a plug-flow type reactor with a custom-made pocket reactor inserted in the large quartz tube (Figure 6.1). The gas inlet is connected to ten mass flow controllers with a range of 10 mL/min to 1500 mL/min that can individually be combined to give the desired gas mixtures and flow rates. The flow reactor can be heated with a heating coil to around 600 °C inside.

The sample itself is placed inside the pocket reactor (inset Figure 6.1). It consists of a rectangular glass pocket with optically flat "windows" (10 mm x 23 mm) connected to a round glass capillary with an inner diameter of 1 mm. The pocket reactor ensures that dilution of reaction products is minimized and enables in this way the use a small amounts of catalyst materials in combination with mass spectrometry in general, and the use of nanofabricated samples as described in chapter 5 in particular. The pocket reactor itself is positioned in the down-stream end of the flow reactor tube such that the incoming gas mixture can be preheated. The quadrupole mass spectrometer (QMS) is a differentially pumped system with a measurement range of 1 u to 200 u.

Two K-typ thermocouples are inserted in the reactor. One is positioned 10 cm down-stream of the gas inlet and the other one is located at the entry of the pocket reactor,

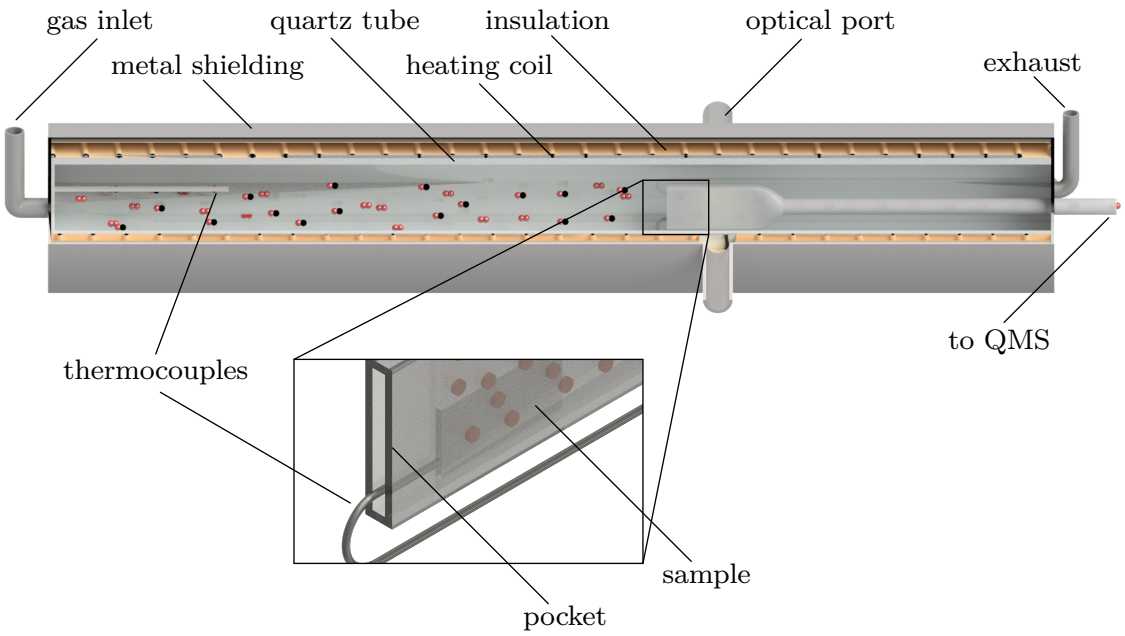

Figure 6.1: The plug flow reactor is an insulated quartz tube that can be heated via a resistive heating coil. It has an optical port that enables illumination for photocatalysis and optical transmittance spectroscopy measurements on each side. The gas inlet is controlled by an array of mass-flow controllers, which can be used to control the desired gas mixture and flow rate. A glass pocket reactor is mounted inside the quartz tube, which hosts the sample. The outlet of the pocket is directly connected to a QMS system. To mount the sample this way ensures that dilution of reaction products is minimized. To control and monitor the temperature of the system two insulated thermocouples are placed inside the reactor, one to monitor the reactor and the other to monitor the sample temperature.

where it touches the sample inside the pocket from the side to accurately measure sample temperature.

The flow reactor itself has an optical port perpendicular to the flow direction, that can be used for optical transmission measurements via fiber coupled spectrometer with 200 nm to 1100 nm spectral range, as well as for illumination in photocatalysis experiments by a high power light source. To this end, the first option is a 250 W quartz tungsten halogen lamp with a high irradiance in the visible and near-infrared

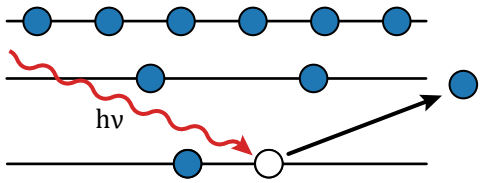

Figure 6.2: The principle of X-ray photoelectron spectroscopy: an incoming X-ray photon kicks out an electron from an inner shell, which is measured by an electron detector. This electron carries information about the elemental composition of the probed surface, as well as about the chemical state of the surface atoms.

spectral range (Osram 64657 HLX lamp in a Newport 67011 housing) and the second option is a 1000 W mercury xenon arc light source that has high irradiance from the middle-ultraviolet to the near-infrared (Newport 6295NS in a 66921 housing). This mercury xenon arc lamp is also equipped with a liquid IR filter that features high transmission in the 250 nm to 950 nm range[86]. Both lamps are further equipped with a condenser lens to ensure a homogeneous illumination of the sample. In **Paper II** I have used the mercury xenon arc light.

6.2 X-ray Photoelectron Spectroscopy

X-ray Photoelectron Spectroscopy (XPS) is a surface sensitive technique that provides information about the chemical state of the surface and enables semi-quantitative analysis of the composition of the sample[87]. Because it gives information about the chemical state of a material it is also called *electron spectroscopy for chemical analysis* (ESCA)[88]. The basic principle of XPS is that the energetic X-rays kick out core electrons of an atom (Figure 6.2), which then can be measured in an electron energy analyzer to draw conclusions about the sample by using a reference library of XPS spectra. The surface sensitivity of XPS arises from the fact that only electrons ejected in the first nanometers from the surface can be measured because that is the mean free path of low energy electrons in matter[89].

Specifically, what is measured in an XPS experiment is the kinetic energy of the electron emitted by the material. To then derive the binding energy of the electron one has to consider which way the electron takes energetically. The electron gets kicked out by a photon with energy, $h\nu$. It has to overcome the binding energy, E_B, and the work function of the sample, Φ_{Sample}. This can be written as

$$h\nu = E_{binding} + \Phi_S + E_{kin,S}\,. \tag{6.1}$$

In Figure 6.3 it can be seen that the equilibrium of the Fermi levels leads to a situation where

$$E_{kin,S} + \Phi_{\text{S}} = E_{kin,XPS} + \Phi_{\text{XPS}}\,. \tag{6.2}$$

Therefore, Equation 6.1 can be written as

$$h\nu = E_{binding} + \Phi_{XPS} + E_{kin,XPS}\,. \tag{6.3}$$

Which in turn leads to the well-known equation for the binding energy

$$E_{binding} = h\nu - \Phi_{XPS} - E_{kin,XPS}\,. \tag{6.4}$$

The instrument itself is comprised of an X-ray source, a monochromator, a sample holder and the electron energy analyzer. The whole system is under UHV to ensure a long mean free path for the electrons on the way from the sample surface to the analyzer .

The X-rays are in most cases generated by accelerating electrons onto a metal target. This leads among others to bremsstrahlung and characteristic emission lines like the K_α-line[91]. These lines are generated by the incoming electron knocking out an electron from an inner shell that gets filled by an electron from an outer shell, thereby emitting a photon. The K_α-line owes its name to the fact that the corresponding knocked-out core electron is located in a K-shell. Most commonly the used targets are magnesium and aluminium due to their narrow full width at half

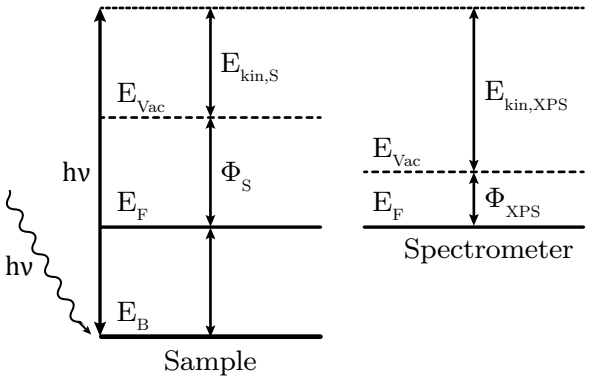

Figure 6.3: A core electron gets kicked out by an irradiated photon with the energy, $h\nu$. It has to overcome the binding energy, E_B, and the work function of the sample, Φ_{Sample}. Upon ejection, it carries the kinetic energy, $E_{kin,S}$.

maximum (fwhm)(0.75 eV and 0.85 eV, respectively)[90], relatively high energy, and intensity of the K_α-line. In cases where higher K_α-energies are needed also silicon, zirconium, silver, titanium or chromium are used but with the drawback of a wider peak. A narrow line width of the X-ray source is important because this is the most important contribution to the energy resolution of the whole system. Next in line is the energy resolution of the energy analyzer and the intrinsic width of photoemission.

The next step after creating the X-rays is the monochromatization, which filters out unnecessary parts of the radiation, like bremsstrahlung, and ensures that only the K_α-line remains. This not only maximizes the resolution of the instrument, due to the narrow fwhm of the remaining K_α-line, but it also removes unnecessary radiation that can degrade the sample. Furthermore, the monochromator also increases the photon flux because, in most cases, it also focuses the beam onto the sample. The monochromator is a concave single crystal that works according to Bragg's law as:

$$n\lambda = 2d \sin \varphi \,. \tag{6.5}$$

Where n is Bragg's reflection order, λ the wavelength of the radiation, d the lattice

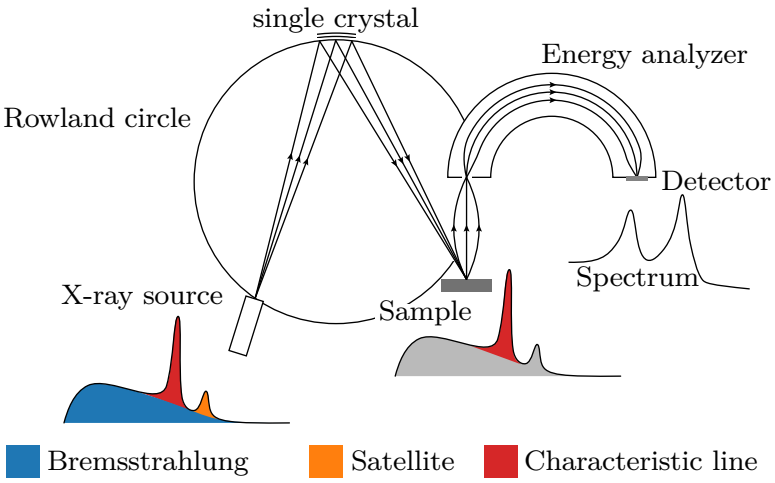

Figure 6.4: The radiation emitted by the X-ray source includes bremsstrahlung, lower intensity characteristic lines (also known as satellites), and the wanted characteristic lines. To filter out the bremsstrahlung and the satellites (monochromatize) a single crystal mirror is used. To focus the X-rays onto the sample, the source, the crystal mirror, and the sample have to be positioned on the so-called Rowland circle. The ejected photoelectrons are measured by an energy analyzer. Adapted from Greczynski and Hultman[91].

distance and φ the reflection angle. To reflect the $Al - K_\alpha$ energy, quartz crystal $\langle 1\,0\,\bar{1}\,0 \rangle$ planes are usually used. However, I want to note that this effect alone only filters the radiation but does not focus it. To focus the X-rays the crystal must be slightly concave and the source and the sample have to be in the correct angle and distance. Specifically, they have to lie on the same imaginary circle, the so called Rowland circle. The whole process is shown in Figure 6.4.

After the X-rays have kicked out an electron from the sample this electron needs to be analyzed in terms of its kinetic energy, in order to derive the binding energy of the electron according to Equation 6.4. There are different kinds of electron energy analyzers, but the most commonly used ones are of the so-called concentric hemispherical type. Such analyzers consist of two concentric hemispherical electrodes. The electrons are then accelerated to a certain energy, the so-called pass energy, and enter the analyzer through a slit to then traverse it on a semicircle trajectory, where they are detected at the end (see right side of Figure 6.4). Depending on the specific

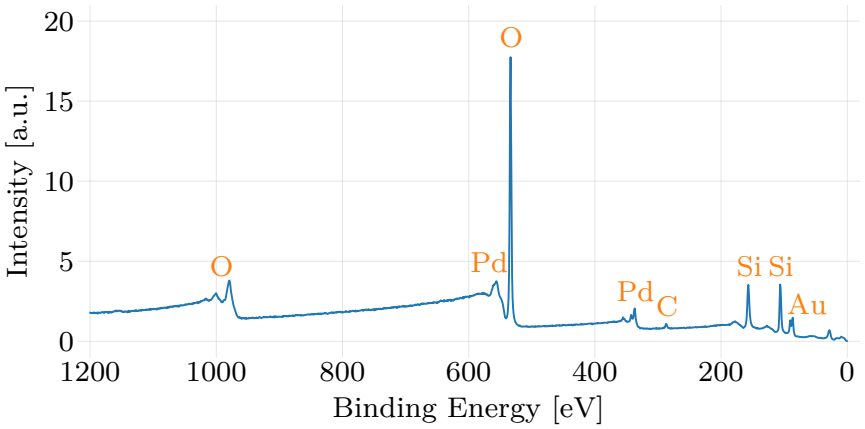

Figure 6.5: A typical XPS-scan of one of my sample surfaces decorated with an array of nanofabricated palladium-gold alloy nanodisks. One can clearly see the respective peaks for gold and palladium. The silicon and oxygen peaks stem from the support material which is oxidized silicon and the carbon peak is due to a thin layer of adventitious carbon.

energy the electrons have, they will have different trajectories and are only detected with the correct energy. This energy filter is used to scan through the whole energy range of interest.

For all this to work, vacuum is needed in the system to ensure that the photoelectrons can travel from the sample to the detector without significant scattering. Another reason why vacuum is important is a clean sample surface since, even if only monolayers of hydrocarbons or water are adsorbed, the measured XPS signal would predominantly stem from this contamination, rather than from the sample itself.

A typical XPS notation for spectral lines gives the element, the principal quantum number, n, the angular quantum number, l, as letter (s,p,d,f), and finally the total angular momentum quantum number, $j = l \pm s$, where s is the spin.

The raw data from an XPS experiment are counts of photoelectrons (intensity) as a function of energy. To translate this into elemental information one can start from theory and the equation that describes the intensity from a core sub-shell, i, for an element, A, with its density, N_A, in small angle $\Delta\Omega$ (typically set by the electron

energy analyzers acceptance angle)[92]

$$I_{A,i} = \frac{\Delta\Omega}{4\pi} \int_0^\infty I_{h\nu}(\alpha, z)\sigma_{A,i}W_{A,i}(\beta_{A,i}, \Psi)N_A(z) \exp\left(-\frac{z}{\lambda_{m,E(A,i)} \cos\theta}\right) dz\,. \tag{6.6}$$

Here z is the in-depth distance from the surface, α the incident angle of the X-ray beam with intensity $I_{h\nu}$, $W_{A,i}(\beta_{A,i}, \Psi)$ the angular asymmetry factor at angle Ψ between X-ray and analyzer, $\sigma_{A,i}$ the total ionization cross section, $\lambda_{m,E(A,i)}$ the effective attenuation length and θ the emission angle of the photoelectrons.

This approach requires in-depth knowledge about the sample and system. Therefore, often a simpler approach is used, invoking the so-called sensitivity factors, S. For an atom, A, the sensitivity factor, S_A, corrects the measured intensity, I_A, to enable extraction of the molar fraction, X_A, via

$$\frac{X_A}{X_B} = \frac{\frac{I_A}{S_A}}{\frac{I_B}{S_B}}\,. \tag{6.7}$$

If one considers a sample composed of N different materials this leads to

$$X_i = \frac{\frac{I_i}{S_i}}{\sum_{j=1}^{N} \frac{I_j}{S_j}} \tag{6.8}$$

$$\sum X_j = 1\,. \tag{6.9}$$

The way the sensitivity factors are derived for different materials can vary. Most commonly, they are obtained by measuring pure reference elements or by deriving the so-called Scofield cross sections, which take into account the energy dependent transmission and attenuation lengths[92].

A typical XPS spectrum obtained by sweeping over the whole energy range is called a survey spectrum and an example of a sample with gold-palladium nanodisks is shown in Figure 6.5. One can clearly see the respective peaks for gold and palladium. The silicon and oxygen peaks stem from the support material of oxidized silicon and the carbon peak is due to a thin layer of adventitious carbon, which is often comprised of polymeric hydrocarbons[93]. This is usually present on any sample that has been exposed to air. Because of its omnipresence it is quite often used as

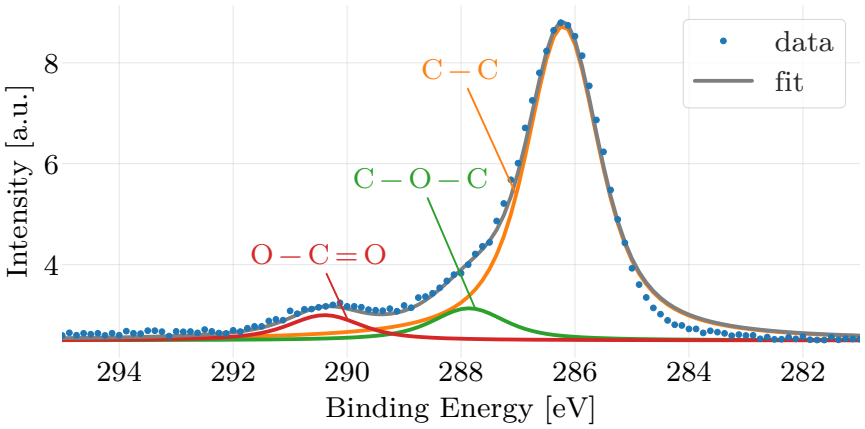

Figure 6.6: The C1s spectrum of adventitious carbon. One can clearly see three different peaks, which provide information about the binding state of the carbon via the chemical shift. Here the strongest peak corresponds to the C–C bond. The secondary peaks correspond to the C–O–C and the O–C=O bonds.

an internal reference for the energy axis of the spectrum. However, this common practice is unfortunately not as reliable as widely assumed, as very recently shown by Greczynski and Hultman[91]. Therefore, referencing of the energy scale needs more careful handling.

The survey-type XPS spectrum typically has a lower energy resolution (lower pass energy and energy steps) and is normally used to get a quick overview of what elements are present in the sample, and a rough estimate of the composition. Especially if all materials are present in a bigger quantity this gives already good results. Subsequently, if more detailed information is required, a closer look with higher energy resolution will provide a more detailed view of sample composition and their chemical state, via so-called chemical shifts. In Figure 6.6 this is shown for the C1s peak, where the strongest peak corresponds to the C–C bond. The secondary peaks correspond to the C–O–C and the O–C=O bonds.

Similarly, looking at a palladium 3d peak, one can see that it is split into two parts (Figure 6.7), due to the spin-orbit-splitting for orbits with an angular momentum $l \neq 0$. Additionally, one can in this example see the contribution of PdO and PdO_2. Finally, it is important to note that it is key for the deconvolution of the

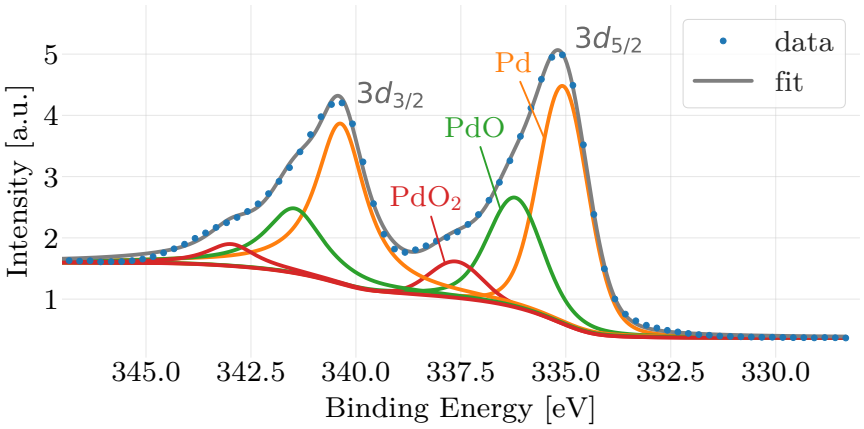

Figure 6.7: The Pd 3d peak is due to spin-orbit splitting divided into $3d_{3/2}$ and $3d_{5/2}$. Additionally one can see a contribution from PdO and PdO_2 on this sample. Further it should be noticed that for this kind of analysis the background from inelastic scattered electron needs to be removed, in this case this was done using the Shirley background.

raw spectrum into constituent peaks to remove the underlying background from the inelastically scattered electrons. The three most common background types are a simple linear approximation, the Shirley background (used in Figure 6.7) and the Tougaard-background. The Shirley background assumes that the background intensity is proportional to the binding energy and the Tougaard background uses the quantitative description of inelastic scattered electrons and is therefore the only background which has a real physical meaning, *i.e.* is not purely empirical. Tougaard and Jansson[94] found that using the Tougaard background offers the highest consistency and validity of the above mentioned background types.

XPS, in **Paper I** and **Paper II**, was utilized to analyze oxidation states single metal nanoparticles and alloy constituents, and to confirm alloy formation after annealing.

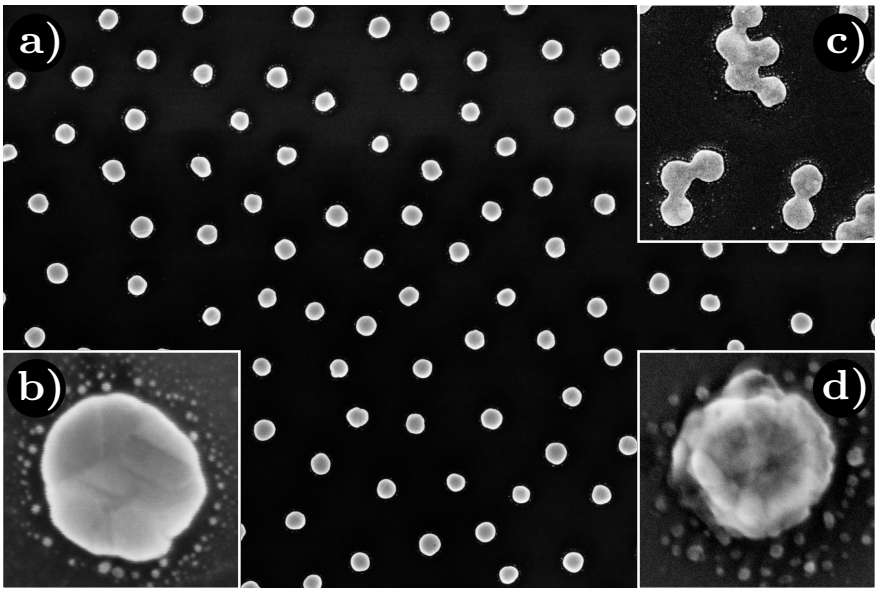

Figure 6.8: SEM images of (an array of) nanofabricated gold-palladium alloy nanodisks as a) an overview of, b) a zoom-in on a single disk, and c) a region with aggregated particles. d) A single copper disk with signs of significant oxidation, as indicated by the rough surface.

6.3 Scanning Electron Microscopy

A scanning electron microscope (SEM) is a setup that can be used to examine the geometry and topography of a sample. The typical spatial resolution is around 1 nm for a conducting specimen but can nowadays easily reach the sub-nanometer limit[95]. SEM is a very popular technique since it is fairly easy to obtain images of good quality and with nanometer resolution. The main purpose of SEM in **Paper I** was to determine the exact geometry and surface coverage of the nanofabricated nanodisks and their arrays, respectively, after annealing (Figure 6.8 a/b). Furthermore, it was also very valuable for the assessment of the condition of the sample in terms of aggregate formation (Figure 6.8c) and oxidation (Figure 6.8d).

A schematic of the electron optics of a SEM is shown in Figure 6.9a. They are comprised of an electron source that provides electrons, up to 30 keV, required for the imaging. Quite often it is a field-emission gun due to the small spot size and high current density it can produce. A system of lenses (condenser and objective lenses)

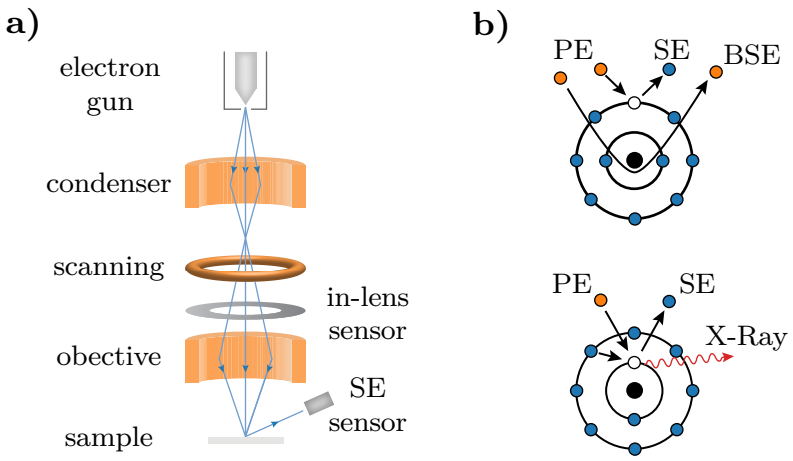

Figure 6.9: (a) Schematic of the electron optics in a SEM. It is comprised of an electron gun, condenser and objective to control density and focus of the electron beam, a scanning coil to be able to scan the beam over the sample, and two sensors to detect the electrons. (b) The three possible scenarios of interaction of the primary electron (PE) beam with the sample surface. Either secondary electrons (SE) are emitted, the PE electrons are back scattered (BSE), or X-rays are produced. The latter can be analyzed in so-called energy-dispersive X-ray analysis (EDX), providing information about the elemental composition of the sample.

are subsequently used to control the beam density and the focus. A third type of lenses are the scan coils. Their task is to raster the beam over the sample to obtain an image of a specific sample area.

The irradiated beam of primary electrons (PE) creates a number of signals upon interaction with the imaged surface: (i) back scattered electrons (BE); (ii) secondary electrons (SE); (iii) Auger electrons; and (iv) X-rays (Figure 6.9b)[96].

BE create an image mainly due to any material contrast in the sample since the backscattering coefficient depends on the element. The heavier the atom is the more it backscatters[96]. Therefore, lighter elements appear darker in the BE-image and heavier elements brighter.

SE are electrons created by ionization of the atoms via the PE beam (Figure 6.9b). They have an energy between a few electron volts to around 50 eV. The SE do not

yield much information about the chemical composition of the sample but instead reveal its topography. Due to their relatively low energy, they origin from within only a few nanometers from the sample surface[96]. For **Paper I** and **Paper II** only secondary electron images were collected.

The created X-rays and Auger electrons can be used for analyzing the chemical elements present in the sample. In case of X-rays, this technique is called Energy-Dispersive X-ray Spectroscopy (EDS or EDX). It provides qualitative and quantitative information about sample composition and, by rastering the PE-beam, elemental maps can be created.

6.4 Transmission Electron Microscopy

Transmission Electron Microscopy (TEM) is similar to SEM but the electrons passing through the sample and are analyzed behind it. This requires higher electron beam energies, typically 50 keV to 200 keV, and thin sample thickness of 10 nm to 100 nm[96]. Because typical nanostructure thicknesses in **Paper I** and **Paper II** are already 25 nm special substrates are needed. Therefore, I used so-called TEM-windows as first introduced by Grant et al.[97]

In **Paper I** and **Paper II** I used TEM in combination with Energy Dispersive X-ray Spectroscopy (EDS or EDXS) to map the elemental composition of my alloy nanostructures with high spatial resolution.

7 Summary and Outlook

7.1 Summary of the Appended Papers

In **Paper I**, we compiled a library of alloy dielectric functions for ten binary alloys based on the late transition metals palladium, platinum, copper, gold, and silver by utilizing time-dependent density-functional theory. We benchmarked the calculated dielectric functions by fabricating series of alloy nanoparticle arrays, measuring their plasmonic properties and comparing these properties with electrodynamic simulations using the derived dielectric functions as the input. As the key result, we found very good agreement between experimentally measured and simulated plasmonic response, and thus corroborated the accuracy and relevance of the calculated library of complex dielectric functions. Seen in a wider context, this provides the community with a uniform and consistent set of dielectric functions of the late transition metal alloys, which are receiving increasing attention in the nanophotonics community. In this context, we predict that they, for example, will make it possible to efficiently screen different alloy compositions and materials without the need of producing a large amount of samples.

In **Paper II**, we investigated photothermal effects as the reaction enhancing mechanism when noble metal catalyst nanoparticles are irradiated with visible light during a catalytic reaction. Specifically, we investigated the significance of the catalytic light-off curve as an important factor to understand reaction rate enhancing mechanisms upon illumination. For this purpose, we alloyed palladium with gold to tailor the catalytic activity in the dark, while, at the same time, maintaining a constant optical cross-section. This way we showed that the catalytic activity is not governed by the photon flux alone but also depends strongly on the catalyst temperature in

the dark. Furthermore, we showed, that alloying can be utilized as a means to tailor the light-off curve of a catalyst to both enhance or suppress the photothermal enhancement channel. Surprisingly, in the field of plasmon mediated catalysis the demonstrated effects are very rarely explicitly taken into account in the assessment discussion of potential reaction rate enhancing mechanisms upon plasmonic catalyst illumination. Therefore, we anticipate that our explicit demonstration of up to three orders of magnitude different photothermal rate enhancement for constant photon flux when moving a catalyst along its light-off curve will raise the necessary awareness in the field of plasmon mediated catalysis and provide novel concepts for the assessment of light-induced catalytic reaction enhancement on plasmonic nanoparticles.

7.2 Outlook

To improve and continue my research in the next years, I can think of several ways on how to do that. The first idea that comes to my mind is to improve the experimental setup to be able to monitor and control more parameters when studying photocatalytic reactions. For example, installing an Iris-Diaphragm on the catalytic reactor would enable me to control the irradiance, while simultaneously maintaining homogeneous illumination of the sample. This way I could see photocatalytic effects that depend on irradiance and provide a further handle to tweak and understand photothermal effects. Additionally, I believe that using a miniaturized reactor would enable better thermal management and more accurate mass spectrometry measurements during a chemical reaction due to reduced dilution of the product.

As a second track, I would like to continue to explore thermal effects in nanoparticles upon illumination, how they can be tweaked and optimized, and in particular how they can be measured accurately. Our two-dimensional samples are perfect candidates for such an endeavor since they reduce the complexity of the system and avoid thermal gradient in the third dimension. Combining my current research with the knowledge acquired by the Langhammer group to use hydride-forming alloy nanopar-

ticles and their ability to sense temperature dependent hydrogen with their LSPR response could open up pathways to do that.

A third interesting route I consider is to explore different alloy combinations with respect to both mixed materials and number of constituents in the context of fundamental nanomaterials science and (photo)catalysis. For example, in **Paper I**, we have touched the topic of ordered intermetallic phases and their optical response. It would be interesting to utilize the theoretical knowledge acquired and apply it to our two-dimensional alloy samples by using them, as in situ optical sensors for monitoring annealing processes or chemical reactions that alter an ordered phase. An interesting candidate in this respect is gold-copper alloys, since this system exhibits several different ordered phases. Furthermore, it is an interesting system for the catalysis of propene epoxidation[98] and benzyl alcohol oxidation[99].

Acknowledgments

First of all, I want to acknowledge the financial support to my project of the Knut and Alice Wallenberg Foundation project 2016.0210 and to the MC2 cleanroom facilities at Chalmers.

A lot of people helped me along the way to achieve this thesis and I want to thank the following people.

First and foremost, I want to thank my supervisor Christoph for the opportunity to do this journey, his guidance, his ability to spark fascination for almost every topic there is.

I also want to thank my co-supervisor Paul for the discussions and my examiner Henrik for his input on this thesis.

Thanks to all my colleagues at chemical physics for a great time at work, outside of Chalmers, at conferences and let's not forget during fika.

Thanks to all members of the Langhammer group and let us not forget about the past ones. Thanks to Stephan, Irem and Arturo for providing a smooth entry in the world of a PhD student and thanks to Zafer and Ferry, which keep up the help even after leaving the group.

Thanks to David and Sara, for discussion and help around FDTD and teaching.

Thanks to my office mates Johan and Olga to make this the best office at Chalmers.

Thanks to Sara for giving me all the nice STEM-EDS images, often with a rather short deadline.

Thanks also to Lars, Lasse and the MC2 cleanroom personal for always getting done what is needed.

Thank you to all my collaborators, at Condensed Matter and Materials Theory, especially Magnus and Tuomas for not getting tired of my questions.

And also, a big thanks to everyone I forgot to mention!

Last but not least I want to thank my wife Kristina, my family and my friends for always supporting me, make life a nice place to be and helping me to endure the more stressful times at work.

Bibliography

[1]T. Bell, *Top steel alloying agents*, https://www.thoughtco.com/common-steel-alloying-agents-properties-and-effects-2340004, (accessed October 11, 2020).

[2]M. Rebello Sousa Dias and M. S. Leite, "Alloying: a platform for metallic materials with on-demand optical response", Accounts of chemical research **52**, 2881–2891 (2019).

[3]I. Chorkendorff and J. W. Niemantsverdriet, *Concepts of modern catalysis and kinetics* (John Wiley & Sons, 2017), ISBN: 9783527305742.

[4]J. Zhang, B. Tian, L. Wang, M. Xing, and J. Lei, *Photocatalysis: fundamentals, materials and applications*, Vol. 100 (Springer, 2018), ISBN: 978-981-13-2113-9.

[5]P. Christopher, H. Xin, and S. Linic, "Visible-light-enhanced catalytic oxidation reactions on plasmonic silver nanostructures", Nature chemistry **3**, 467–472 (2011).

[6]S. Mukherjee, F. Libisch, N. Large, O. Neumann, L. V. Brown, J. Cheng, J. B. Lassiter, E. A. Carter, P. Nordlander, and N. J. Halas, "Hot electrons do the impossible: Plasmon-induced dissociation of H 2 on Au", Nano Letters **13**, 240–247 (2013).

[7]S. Linic, U. Aslam, C. Boerigter, and M. Morabito, "Photochemical transformations on plasmonic metal nanoparticles", Nature materials **14**, 567–576 (2015).

[8]Y. Sivan, I. W. Un, and Y. Dubi, "Assistance of metal nanoparticles in photocatalysis–nothing more than a classical heat source", Faraday discussions **214**, 215–233 (2019).

[9]L. Zhou, D. F. Swearer, C. Zhang, H. Robatjazi, H. Zhao, L. Henderson, L. Dong, P. Christopher, E. A. Carter, P. Nordlander, and N. J. Halas, "Quantifying hot carrier and thermal contributions in plasmonic photocatalysis", Science **362**, 69–72 (2018).

[10]F. Habashi, *Alloys: preparation, properties, applications* (John Wiley & Sons, 2008), ISBN: 978-3-527-61192-8.

[11]W. D. Callister and D. G. Rethwisch, *Materials science and engineering: an introduction*, Vol. 9 (Wiley New York, 2018), ISBN: 978-1-119-40549-8.

[12]H. Okamoto, M. Schlesinger, and E. Mueller, *Alloy Phase Diagrams* (ASM International, 2016), ISBN: 978-1-62708-163-4.

[13]U. Mizutani, *Hume-rothery rules for structurally complex alloy phases* (CRC Press, 2016), ISBN: 9781420090598.

[14]A. Kawecki, T. Knych, E. Sieja-Smaga, A. Mamala, P. Kwaśniewski, G. Kiesiewicz, B. Smyrak, and A Pacewicz, "Fabrication, properties and microstructures of high strength and high conductivity copper-silver wires", Archives of Metallurgy and Materials **57** (2013).

[15]D. Salgado and R. Lillard, "Metal salt solutions as a simulant for the chemistry in crevices of nickel alloy 625", Journal of The Electrochemical Society **164**, C801 (2017).

[16]S. Ghosh, A. Grover, G. Dey, and M. Totlani, "Nanocrystalline ni–cu alloy plating by pulse electrolysis", Surface and Coatings Technology **126**, 48–63 (2000).

[17]K. Upadhya, "Thermodynamics and kinetics of simultaneous reduction of nickel oxide by iron and carbon to produce ni-fe alloys", Journal of materials engineering **13**, 29–37 (1991).

[18]P.-Y. Silvert, V Vijayakrishnan, P Vibert, R Herrera-Urbina, and K. Elhsissen, "Synthesis and characterization of nanoscale ag-pd alloy particles", Nanostructured materials **7**, 611–618 (1996).

[19]M. Bala, S. Gupta, T. S. Tripathi, S. K. Tripathi, K Asokan, D. K. Avasthi, et al., "Phase evolution and electrical properties of co–sb alloys fabricated from co/sb bilayers by thermal annealing and ion beam mixing", Physical Chemistry Chemical Physics **17**, 24427–24437 (2015).

[20]F. A. A. Nugroho, B. Iandolo, J. B. Wagner, and C. Langhammer, "Bottom-Up Nanofabrication of Supported Noble Metal Alloy Nanoparticle Arrays for Plasmonics", ACS Nano **10**, 2871–2879 (2016).

[21]F. C. Campbell, *Elements of Metallurgy and Engineering Alloys* (ASM International, Materials Park, United States, 2008), ISBN: 9781615030583.

[22]M. Zhao, W. G. Sloof, and A. J. Böttger, "Modelling of surface segregation for palladium alloys in vacuum and gas environments", International Journal of Hydrogen Energy **43**, 2212–2223 (2018).

[23]D. Raabe, "23 - recovery and recrystallization: phenomena, physics, models, simulation", in *Physical metallurgy (fifth edition)*, edited by D. E. Laughlin and K. Hono, Fifth Edition (Elsevier, Oxford, 2014), pp. 2291 –2397, ISBN: 978-0-444-53770-6.

[24]H. L. Skriver and N. M. Rosengaard, "Surface energy and work function of elemental metals", Physical Review B **46**, 7157–7168 (1992).

[25]S. Zafeiratos, S. Piccinin, and D. Teschner, "Alloys in catalysis: Phase separation and surface segregation phenomena in response to the reactive environment", Catalysis Science and Technology **2**, 1787–1801 (2012).

[26]K. J. Andersson, F. Calle-Vallejo, J. Rossmeisl, and I. Chorkendorff, "Adsorption-driven surface segregation of the less reactive alloy component", Journal of the American Chemical Society **131**, 2404–2407 (2009).

[27]S. A. Maier, *Plasmonics: fundamentals and applications* (Springer Science & Business Media, 2007), ISBN: 978-0-387-37825-1.

[28]P. B. Johnson and R. W. Christy, "Optical constants of the noble metals", Phys. Rev. B **6**, 4370–4379 (1972).

[29]U. Kreibig and M. Vollmer, *Optical properties of metal clusters*, Vol. 25 (Springer Science & Business Media, 2013), ISBN: 978-3-662-09109-8.

[30]T. Rangel, D Kecik, P. Trevisanutto, G.-M. Rignanese, H Van Swygenhoven, and V. Olevano, "Band structure of gold from many-body perturbation theory", Physical Review B **86**, 125125 (2012).

[31]C. F. Bohren and D. R. Huffman, *Absorption and scattering of light by small particles* (John Wiley & Sons, 2008), ISBN: 9780471293408.

[32]R. C. Rumpf, *Electromagnetic analysis using finite-difference time-domain*, 2019.

[33]Kane Yee, "Numerical solution of initial boundary value problems involving maxwell's equations in isotropic media", IEEE Transactions on Antennas and Propagation **14**, 302–307 (1966).

[34]W. Yu, *Advanced fdtd methods: parallelization, acceleration, and engineering applications* (Artech House, 2011), ISBN: 9781608071760.

[35]S. Enoch, R. Quidant, and G. Badenes, "Optical sensing based on plasmon coupling in nanoparticle arrays", Optics express **12**, 3422–3427 (2004).

[36]T. J. Antosiewicz, S. P. Apell, M. Zäch, I. Zorić, and C. Langhammer, "Oscillatory optical response of an amorphous two-dimensional array of gold nanoparticles", Physical review letters **109**, 247401 (2012).

[37]E. D. Palik, *Handbook of optical constants of solids*, Vol. 3 (Academic press, 1998), ISBN: 978-0-12-544422-4.

[38]J. M. Rahm, C. Tiburski, T. P. Rossi, F. A. A. Nugroho, S. Nilsson, C. Langhammer, and P. Erhart, "A library of late transition metal alloy dielectric functions for nanophotonic applications", Advanced Functional Materials **30**, 2002122 (2020).

[39]I. H. Malitson, "Interspecimen comparison of the refractive index of fused silica", Josa **55**, 1205–1209 (1965).

[40]R. L. Olmon, B. Slovick, T. W. Johnson, D. Shelton, S.-H. Oh, G. D. Boreman, and M. B. Raschke, "Optical dielectric function of gold", Phys. Rev. B **86**, 235147 (2012).

[41]C. Persson, A. F. da Silva, R Ahuja, and B. Johansson, "First-principle calculations of the dielectric function of zinc-blende and wurtzite inn", Journal of Physics: Condensed Matter **13**, 8945 (2001).

[42]I. Zoric, M. Zach, B. Kasemo, and C. Langhammer, "Gold, platinum, and aluminum nanodisk plasmons: material independence, subradiance, and damping mechanisms", ACS nano **5**, 2535–2546 (2011).

[43]D. Rioux, S. Vallières, S. Besner, P. Muñoz, E. Mazur, and M. Meunier, "An analytic model for the dielectric function of au, ag, and their alloys", Advanced Optical Materials **2**, 176–182 (2014).

[44]S. K. F. Stofela, O. Kizilkaya, B. T. Diroll, T. R. Leite, M. M. Taheri, D. E. Willis, J. B. Baxter, W. A. Shelton, P. T. Sprunger, and K. M. McPeak, "A noble-transition alloy excels at hot-carrier generation in the near infrared", Advanced Materials **32**, 1906478 (2020).

[45]S. Babar and J. H. Weaver, "Optical constants of cu, ag, and au revisited", Appl. Opt. **54**, 477–481 (2015).

[46]A. Ciesielski, L. Skowronski, M. Trzcinski, E. Górecka, P. Trautman, and T. Szoplik, "Evidence of germanium segregation in gold thin films", Surface Science **674**, 73 –78 (2018).

[47]H.-J. Hagemann, W. Gudat, and C. Kunz, "Optical constants from the far infrared to the x-ray region: mg, al, cu, ag, au, bi, c, and al2o3", J. Opt. Soc. Am. **65**, 742–744 (1975).

[48]F. Lemarchand, L. Gao, and M. Lequime, "Comparison of different dispersion models for single layer optical thin film index determination", Thin Solid Films **520**, 501 –509 (2011).

[49]K. M. McPeak, S. V. Jayanti, S. J. P. Kress, S. Meyer, S. Iotti, A. Rossinelli, and D. J. Norris, "Plasmonic films can easily be better: rules and recipes", ACS Photonics **2**, 326–333 (2015).

[50]D. L. Windt, W. C. Cash, M. Scott, P. Arendt, B. Newnam, R. F. Fisher, and A. B. Swartzlander, "Optical constants for thin films of ti, zr, nb, mo, ru, rh, pd, ag, hf, ta, w, re, ir, os, pt, and au from 24 Å to 1216 Å", Appl. Opt. **27**, 246–278 (1988).

[51]D. I. Yakubovsky, A. V. Arsenin, Y. V. Stebunov, D. Y. Fedyanin, and V. S. Volkov, "Optical constants and structural properties of thin gold films", Optics Express **25**, 25574 (2017).

[52]K. M. McPeak, S. V. Jayanti, S. J. Kress, S. Meyer, S. Iotti, A. Rossinelli, and D. J. Norris, "Plasmonic films can easily be better: Rules and recipes", ACS Photonics **2**, 326–333 (2015).

[53]M Gaudry, J Lermé, E Cottancin, M Pellarin, J.-L. Vialle, M Broyer, B Prével, M Treilleux, and P Mélinon, "Optical properties of (au x ag 1- x) n clusters embedded in alumina: evolution with size and stoichiometry", Physical Review B **64**, 085407 (2001).

[54]A. Zunger, S.-H. Wei, L. Ferreira, and J. E. Bernard, "Special quasirandom structures", Physical Review Letters **65**, 353 (1990).

[55]J. K. Nørskov, J. Rossmeisl, A. Logadottir, L. Lindqvist, J. R. Kitchin, T. Bligaard, and H. Jónsson, "Origin of the overpotential for oxygen reduction at a fuel-cell cathode", Journal of Physical Chemistry B **108**, 17886–17892 (2004).

[56]Y. F. Han, J. H. Wang, D. Kumar, Z. Yan, and D. W. Goodman, "A kinetic study of vinyl acetate synthesis over Pd-based catalysts: Kinetics of vinyl acetate synthesis over Pd-Au/SiO2 and Pd/SiO 2 catalysts", Journal of Catalysis **232**, 467–475 (2005).

[57]F. Garin, "Environmental catalysis", Catalysis Today **89**, 255–268 (2004).

[58]F. Besenbacher, I. Chorkendorff, B. S. Clausen, B. Hammer, A. M. Molenbroek, J. K. Nørskov, and I. Stensgaard, "Design of a surface alloy catalyst for steam reforming", Science **279**, 1913–1915 (1998).

[59]A. Naldoni, F. Riboni, U. Guler, A. Boltasseva, V. M. Shalaev, and A. V. Kildishev, *Solar-Powered Plasmon-Enhanced Heterogeneous Catalysis*, 2016.

[60]M. L. Brongersma, N. J. Halas, and P. Nordlander, "Plasmon-induced hot carrier science and technology", Nature Nanotechnology **10**, 25–34 (2015).

[61]Z. Liu, W. Hou, P. Pavaskar, M. Aykol, and S. B. Cronin, "Plasmon resonant enhancement of photocatalytic water splitting under visible illumination", Nano Letters **11**, 1111–1116 (2011).

[62]T. P. Rossi, M. Kuisma, M. J. Puska, R. M. Nieminen, and P. Erhart, "Kohn-Sham Decomposition in Real-Time Time-Dependent Density-Functional Theory: An Efficient Tool for Analyzing Plasmonic Excitations", (2017).

[63]A. Manjavacas, J. G. Liu, V. Kulkarni, and P. Nordlander, "Plasmon-induced hot carriers in metallic nanoparticles", ACS Nano **8**, 7630–7638 (2014).

[64]T. P. Rossi, P. Erhart, and M. Kuisma, "Hot-carrier generation in plasmonic nanoparticles: Atomic-scale structure matters", (2020).

[65]K. Li, N. J. Hogan, M. J. Kale, N. J. Halas, P. Nordlander, and P. Christopher, "Balancing Near-Field Enhancement, Absorption, and Scattering for Effective Antenna-Reactor Plasmonic Photocatalysis", Nano Letters **17**, 3710–3717 (2017).

[66]G. Baffou, I. Bordacchini, A. Baldi, and R. Quidant, "Simple experimental procedures to distinguish photothermal from hot-carrier processes in plasmonics", Light: Science & Applications **9**, 108 (2020).

[67]J. Aizpurua, F. Baletto, J. Baumberg, P. Christopher, B. De Nijs, P. Deshpande, Y. D. Fernandez, L. Fabris, S. Freakley, S. Gawinkowski, et al., "Theory of hot electrons: general discussion", Faraday discussions **214**, 245–281 (2019).

[68]US Deparnnent of Health and Human Services - Centers for Disease Control and Prevention National - Institute for Occupational Safety and Health, *Niosh pocket guide to chemical hazards*, 2007.

[69]World Health Organization, *Monitoring ambient air quality for health impact assessment* (Copenhagen: WHO Regional Office for Europe, 1999), ISBN: 9789289013512.

[70]National Center for Environmental Health, *Carbon monoxide poisoning*, `https://www.cdc.gov/co/faqs.htm`, (accessed: 30.06.2020).

[71]Drägerwerk AG & Co. KGaA, *Leitfaden zur filterauswahl*, `https://www.draeger.com/products/content/ab-filter-selection-guide-fl-9046528-de-de.pdf`, (accessed: 30.06.2020).

[72]N. K. Soliman, *Factors affecting CO oxidation reaction over nanosized materials: A review*, 2019.

[73]A. C. Garcia, V. A. Paganin, and E. A. Ticianelli, "Co tolerance of pdpt/c and pdptru/c anodes for pemfc", Electrochimica Acta **53**, 4309–4315 (2008).

[74]J. T. Kummer, "Use of noble metals in automobile exhaust catalysts", Journal of Physical Chemistry **90**, 4747–4752 (1986).

[75]T.-J. Huang and D.-H. Tsai, "Co oxidation behavior of copper and copper oxides", Catalysis Letters **87**, 173–178 (2003).

[76]A. Biabani-Ravandi and M. Rezaei, "Low temperature co oxidation over fe–co mixed oxide nanocatalysts", Chemical Engineering Journal **184**, 141–146 (2012).

[77]M. Haruta, T. Kobayashi, H. Sano, and N. Yamada, "Novel gold catalysts for the oxidation of carbon monoxide at a temperature far below 0 c", Chemistry Letters **16**, 405–408 (1987).

[78]R. F. Baddour, M. Modell, and U. K. Heusser, "Simultaneous kinetic and infrared spectral studies of carbon monoxide oxidation on palladium under steady-state conditions", The Journal of Physical Chemistry **72**, 3621–3629 (1968).

[79]A. M. Venezia, V. La Parola, G Deganello, B Pawelec, and J. L. Fierro, "Synergetic effect of gold in Au/Pd catalysts during hydrodesulfurization reactions of model compounds", Journal of Catalysis **215**, 317–325 (2003).

[80]J. K. Edwards, B. E. Solsona, P. Landon, A. F. Carley, A. Herzing, C. J. Kiely, and G. J. Hutchings, "Direct synthesis of hydrogen peroxide from H2 and O2 using TiO2-supported Au-Pd catalysts", Journal of Catalysis **236**, 69–79 (2005).

[81]A Beck, A. Horváth, Z Schay, G. Stefler, Z. Koppány, I Sajó, O Geszti, and L Guczi, "Sol derived gold-palladium bimetallic nanoparticles on TiO2: Structure and catalytic activity in CO oxidation", Topics in Catalysis **44**, 115–121 (2007).

[82]H. Fredriksson, Y. Alaverdyan, A. Dmitriev, C. Langhammer, D. S. Sutherland, M. Zäch, and B. Kasemo, "Hole–mask colloidal lithography", Advanced Materials **19**, 4297–4302 (2007).

[83]Z. Cui, *Nanofabrication: Principles, Capabilities and Limits: Second Edition* (2017), pp. 1–432, ISBN: 9783319393612.

[84]S. Syrenova, C. Wadell, and C. Langhammer, "Shrinking-hole colloidal lithography: self-aligned nanofabrication of complex plasmonic nanoantennas", Nano letters **14**, 2655–2663 (2014).

[85]M. Pal, J Garcia Serrano, P Santiago, and U Pal, "Size-controlled synthesis of spherical tio2 nanoparticles: morphology, crystallization, and phase transition", The Journal of Physical Chemistry C **111**, 96–102 (2007).

[86]Newport Corporation, *Liquid filters for light sources*, `https://www.newport.com/f/liquid-filters`, (accessed: 11.09.2020).

[87]J. F. Moulder, W. F. Stickle, P. E. Sobol, and K. D. Bomben, *Handbook of x-ray photoelectron spectroscopy: a reference book of standard spectra for identification and interpretation of xps data; physical electronics: eden prairie, mn, 1995* (1995), ISBN: 978-0964812413.

[88]K. Siegbahn, "Esca: atomic, molecular and solid state structure studies by means of electron spectroscopy; pres. to the royal society of sciences of uppsala, dec. 3rd, 1965", Nova Acta Regiae Societatis Scientiarum Upsaliensis (1967).

[89]S. Tanuma, C. J. Powell, and D. R. Penn, "Calculations of electron inelastic mean free paths (imfps). iv. evaluation of calculated imfps and of the predictive imfp formula tpp-2 for electron energies between 50 and 2000 ev", Surface and Interface Analysis **20**, 77–89 (1993).

[90]A. F. Lee, C. M. Parlett, and K. Wislon, *X-ray photoelectron spectroscopy*, 2017.

[91]G. Greczynski and L. Hultman, "X-ray photoelectron spectroscopy: towards reliable binding energy referencing", Progress in Materials Science **107**, 100591 (2020).

[92]S. Hofmann, *Auger-and x-ray photoelectron spectroscopy in materials science: a user-oriented guide*, Vol. 49 (Springer Science & Business Media, 2012), ISBN: 978-3-642-27381-0.

[93]T. L. Barr and S. Seal, "Nature of the use of adventitious carbon as a binding energy standard", Journal of Vacuum Science & Technology A: Vacuum, Surfaces, and Films **13**, 1239–1246 (1995).

[94]S Tougaard and C Jansson, "Comparison of validity and consistency of methods for quantitative xps peak analysis", Surface and interface analysis **20**, 1013–1046 (1993).

[95]Carl Zeiss Microscopy GmbH, *Zeiss geminisem*, `https://www.zeiss.com/microscopy/int/products/scanning-electron-microscopes/geminisem.html`, (accessed: 13.07.2020).

[96]K. Oura, V. Lifshits, A. Saranin, A. Zotov, and M Katayama, *Surface science: an introduction* (Springer Science & Business Media, 2013), ISBN: 978-3-662-05179-5.

[97]A. W. Grant, Q.-H. Hu, and B Kasemo, "Transmission electron microscopy windows for nanofabricated structures", Nanotechnology **15**, 1175–1181 (2004).

[98]R. Chimentao, F Medina, J. Fierro, J Llorca, J. Sueiras, Y Cesteros, and P Salagre, "Propene epoxidation by nitrous oxide over au–cu/tio2 alloy catalysts", Journal of Molecular Catalysis A: Chemical **274**, 159–168 (2007).

[99]C. Della Pina, E. Falletta, and M. Rossi, "Highly selective oxidation of benzyl alcohol to benzaldehyde catalyzed by bimetallic gold–copper catalyst", Journal of Catalysis **260**, 384–386 (2008).